Physics of Plasmas

Propagation properties of electron cyclotron waves with helical wavefronts in magnetized plasma

Cite as: Phys. Plasmas **28**, 012502 (2021); https://doi.org/10.1063/5.0015109
Submitted: 25 May 2020 • Accepted: 10 December 2020 • Published Online: 06 January 2021

Toru Ii Tsujimura and Shin Kubo

Physics of Plasmas ARTICLE scitation.org/journal/php

Propagation properties of electron cyclotron waves with helical wavefronts in magnetized plasma

Cite as: Phys. Plasmas **28**, 012502 (2021); doi: 10.1063/5.0015109
Submitted: 25 May 2020 · Accepted: 10 December 2020 ·
Published Online: 6 January 2021

Toru Ii Tsujimura[a] and Shin Kubo

AFFILIATIONS

National Institute for Fusion Science, National Institutes of Natural Sciences, Toki, Gifu 509-5292, Japan

[a]Author to whom correspondence should be addressed: tsujimura.tohru@nifs.ac.jp

ABSTRACT

Propagation properties of an optical vortex with a helical wavefront in cold uniform magnetized plasma are theoretically investigated in an electron cyclotron range of frequencies. The effects of the helical wavefront of the optical vortex on the wave fields in magnetized plasma are described. These effects become significant as the topological charge of the optical vortex increases or the distance from the phase singularity point becomes small. The different properties of propagation are also confirmed in propagation of Laguerre–Gaussian beams by three-dimensional simulations with the finite element method.

I. INTRODUCTION

Radiofrequency (RF) waves are widely employed for heating, current drive, and diagnostics in magnetic fusion plasma. Knowledge of the propagation properties of RF waves in magnetized plasma is fundamental to designs of RF systems such as launching antennas. The propagation properties of RF waves conventionally originate from a plane wave. In other words, the phase of the wave fields is assumed to be $\boldsymbol{k}\cdot\boldsymbol{r}-\omega t$,[1] where $\boldsymbol{k}$, $\boldsymbol{r}$, ω, and t denote a wave vector, a position vector, an angular frequency, and time. This expression is a simple way, adopted in many textbooks, to introduce this topic, although advanced methods for the description of wave beams in dispersive media have progressed.[2]

Recently, it is theoretically demonstrated that a single free electron in circular or spiral motion emits twisted photons carrying orbital angular momentum (OAM) along the axis of the electron circulation, in addition to spin angular momentum.[3] It is found that the radiated wave field has a phase term represented by $l\varphi+k_z z-\omega t$, where l is the topological charge and φ is the azimuthal angle around the propagation axis z. The wave with a helical wavefront is commonly called an optical vortex. An optical vortex was originally discussed regarding a special mode of electromagnetic waves called the Laguerre–Gaussian (LG) mode[4] and was conventionally considered to be produced artificially with optical elements.[5] However, the twisted photons are naturally emitted by cyclotron motion of electrons and are more ubiquitous in laboratories and in nature than ever thought.[6–8]

Naturally, questions arise as to how an optical vortex propagates in magnetized plasma and whether the unique property of the helical wavefront is beneficial to heating, current drive, or diagnostics in magnetic fusion plasma.[9–11] In this paper, propagation properties of an optical vortex are discussed theoretically and numerically for an electron cyclotron (EC) range of frequencies in cold uniform magnetized plasma. Section II theoretically describes propagation properties of EC waves with helical wavefronts in cold uniform magnetized plasma. Results on three-dimensional (3D) simulations for propagation of LG beams are presented and discussed in Sec. III. Section IV summarizes this paper with a future outlook.

II. PROPAGATION PROPERTIES OF AN EC WAVE WITH A HELICAL WAVEFRONT IN COLD UNIFORM MAGNETIZED PLASMA

A. Wave with a helical wavefront

The Maxwell equations in magnetized plasma are given by

$$\begin{aligned}\nabla\times\boldsymbol{E}&=-\frac{\partial\boldsymbol{B}}{\partial t},\\ \nabla\times\boldsymbol{B}&=\mu_0\left(\boldsymbol{j}+\varepsilon_0\frac{\partial\boldsymbol{E}}{\partial t}\right).\end{aligned}\tag{1}$$

Assuming a monochromatic wave in time represented with the term $e^{\mp i\omega t}$ and using the dielectric tensor operator $\boldsymbol{\varepsilon}_r$, which is given later, in magnetized plasma, Eq. (1) can be rewritten as

$$\nabla \times (\nabla \times \boldsymbol{E}) - k_0^2 \boldsymbol{\varepsilon}_r \cdot \boldsymbol{E} = \boldsymbol{0}, \tag{2}$$

where k_0 is the wavenumber in the vacuum. In contrast to a plane wave, one should start with a sufficiently general ansatz for the wave field of an optical vortex. The electric field of an optical vortex is assumed to be given by

$$\begin{aligned}\boldsymbol{E}(r,\varphi,z) &= \frac{1}{2}\left\{\tilde{\boldsymbol{E}}(r,\varphi,z)\alpha r^{|l|}\exp\left[\mathrm{i}(l\varphi+\psi(r,\varphi,z)-\omega t)\right] + \text{c.c.}\right\} \\ &= \frac{1}{2}\left\{\tilde{\boldsymbol{E}}\alpha r^{|l|}\exp\left[\mathrm{i}(l\varphi+\psi-\omega t)\right]\right. \\ &\quad \left. +\tilde{\boldsymbol{E}}^*\alpha^* r^{|l|}\exp\left[\mathrm{i}(-l\varphi-\psi^*+\omega t)\right]\right\},\end{aligned} \tag{3}$$

where

$$\psi(r,\varphi,z) = \int_0^z k_z(r,\varphi,z')\mathrm{d}z'$$

is a complex-valued phase function with $k_z = \partial_z\psi$ the z component of the local wave vector. Here, the solution for k_z is in the end a complex-valued function of both r and φ. The electric field amplitude $\tilde{\boldsymbol{E}}$ is complex vector-valued, which includes the polarization. A constant α is to arrange the unit of the electric field. Then, $\boldsymbol{E}$ becomes a real electric field vector. When $\tilde{\boldsymbol{E}}$ and k_z are constant on space, this simple form of the optical vortex satisfies the Maxwell equations in the vacuum without any approximation.[12] Due to the factor, $r^{|l|}$, the amplitude at the phase singularity point, i.e., at $r=0$, is zero, which is a requirement of optical vortices. Here, by putting $s = \alpha r^{|l|}\exp\left[\mathrm{i}(l\varphi+\psi-\omega t)\right]$,

$$\boldsymbol{\varepsilon}_r(\omega)\cdot\boldsymbol{E} = \frac{1}{2}\left\{\boldsymbol{\varepsilon}_r(\omega)\cdot\tilde{\boldsymbol{E}}s + \boldsymbol{\varepsilon}_r^*(-\omega)\cdot\tilde{\boldsymbol{E}}^* s^*\right\}$$

can be obtained based on the identity $\boldsymbol{\varepsilon}_r(\omega) = \boldsymbol{\varepsilon}_r^*(-\omega)$ which is satisfied by the cold plasma dielectric tensor. The complex conjugate s^* corresponds to the angular frequency $-\omega$.

The standard approach in complex eikonal theory requires that the amplitude $\tilde{\boldsymbol{E}}$ is weakly varying. In ordering assumptions, there is a characteristic scale length L_0 such that

$$\epsilon = \frac{\lambda_0}{L_0} \ll 1 \tag{4}$$

and

$$\frac{|\nabla\tilde{E}_\sigma|}{|\tilde{\boldsymbol{E}}|} \sim \frac{1}{L_0}, \quad \frac{|\nabla\times(\nabla\times\tilde{\boldsymbol{E}})|}{|\tilde{\boldsymbol{E}}|} \sim \frac{1}{L_0^2}$$

for all components $\sigma = x, y, z$. Here, λ_0 is the wavelength in the vacuum. In uniform plasma where both a static magnetic field and electron density are constant on space, the scale length L_0 is defined by the variations of the amplitude $\tilde{\boldsymbol{E}}$ and the short wavelength condition given by Eq. (4). Then, let us perform

$$\begin{aligned}\nabla E_\sigma &\approx \frac{1}{2}\left\{\mathrm{i}\left(-\mathrm{i}\frac{|l|}{r}\nabla r + l\nabla\varphi + k_z\nabla z\right)\tilde{E}_\sigma s\right. \\ &\quad \left. -\mathrm{i}\left(\mathrm{i}\frac{|l|}{r}\nabla r + l\nabla\varphi + k_z^*\nabla z\right)\tilde{E}_\sigma^* s^*\right\} \\ &= \frac{1}{2}\left\{\mathrm{i}\left(-\mathrm{i}\frac{|l|}{r}\boldsymbol{e}_r + \frac{l}{r}\boldsymbol{e}_\varphi + k_z\boldsymbol{e}_z\right)\tilde{E}_\sigma s\right. \\ &\quad \left. -\mathrm{i}\left(\mathrm{i}\frac{|l|}{r}\boldsymbol{e}_r + \frac{l}{r}\boldsymbol{e}_\varphi + k_z^*\boldsymbol{e}_z\right)\tilde{E}_\sigma^* s^*\right\} \\ &= \frac{1}{2}\left\{\mathrm{i}\begin{pmatrix}-\mathrm{i}\dfrac{|l|}{r\mathrm{e}^{\mathrm{isgn}(l)\varphi}}\boldsymbol{e}_x \\ +\dfrac{l}{r\mathrm{e}^{\mathrm{isgn}(l)\varphi}}\boldsymbol{e}_y \\ +k_z\boldsymbol{e}_z\end{pmatrix}\tilde{E}_\sigma s - \mathrm{i}\begin{pmatrix}\mathrm{i}\dfrac{|l|}{r\mathrm{e}^{-\mathrm{isgn}(l)\varphi}}\boldsymbol{e}_x \\ +\dfrac{l}{r\mathrm{e}^{-\mathrm{isgn}(l)\varphi}}\boldsymbol{e}_y \\ +k_z^*\boldsymbol{e}_z\end{pmatrix}\tilde{E}_\sigma^* s^*\right\}\end{aligned}$$

$(\sigma = x, y, z).$

This formula suggests that the "wave vector" of the optical vortex with a helical wavefront can be expressed as

$$\begin{aligned}\boldsymbol{k} &= -\mathrm{i}\frac{|l|}{r}\nabla r + l\nabla\varphi + k_z(r,\varphi,z)\nabla z \\ &= -\mathrm{i}\frac{|l|}{r}\boldsymbol{e}_r + \frac{l}{r}\boldsymbol{e}_\varphi + k_z\boldsymbol{e}_z \\ &= -\mathrm{i}\frac{|l|}{r\mathrm{e}^{\mathrm{isgn}(l)\varphi}}\boldsymbol{e}_x + \frac{l}{r\mathrm{e}^{\mathrm{isgn}(l)\varphi}}\boldsymbol{e}_y + k_z\boldsymbol{e}_z.\end{aligned} \tag{5}$$

Clearly, there is a singularity at $r=0$ in both the first two terms on the right-hand side. In the ordering assumptions, the phase singularity is a delicate point. A simple approach here is to exclude the propagation axis $r=0$. The description of the wave field is restricted in the region $r \geq r_0 > 0$. In the region $r \geq r_0$, a natural approach would be to look for a solution such that

$$|\boldsymbol{k}| \sim |k_z| \sim k_0 = \frac{2\pi}{\lambda_0}, \quad |\nabla k_\sigma| \sim \frac{k_0}{L_0}$$

for all components $\sigma = x, y, z$. Since it can be written that

$$|\boldsymbol{k}|^2 = \frac{2l^2}{r^2} + |k_z|^2 \leq \frac{2l^2}{r_0^2} + |k_z|^2,$$

the condition $|\boldsymbol{k}| \sim 2\pi/\lambda_0$ leads to

$$|k_z| \sim k_0 = \frac{2\pi}{\lambda_0}$$

and

$$\begin{aligned}&\frac{l^2}{r_0^2} \leq \frac{4\pi^2}{\lambda_0^2}, \\ &\therefore \quad r_0 \geq \frac{|l|}{2\pi}\lambda_0.\end{aligned} \tag{6}$$

For the gradients of the complex wave vector, it can be written that

$$\nabla \boldsymbol{k} = \frac{\partial k_z}{\partial r}\nabla r \otimes \nabla z + \frac{\partial k_z}{\partial \varphi}\nabla \varphi \otimes \nabla z + \frac{\partial k_z}{\partial z}\nabla z \otimes \nabla z + i\frac{|l|}{r^2}\nabla r \otimes \nabla r + l\nabla\nabla\varphi - i\frac{|l|}{r}\nabla\nabla r$$

and $\nabla\nabla r \sim 1/r$, $\nabla\nabla\varphi \sim 1/r^2$. Here, the symbol $\otimes$ denotes the dyadic operator. In order to enforce $|\nabla k_\sigma| \sim k_0/L_0$, it must be assumed that

$$\left|\frac{\partial k_z}{\partial r}\right| \sim \frac{k_0}{L_0}, \quad \left|\frac{\partial k_z}{\partial \varphi}\right| \sim \frac{k_0 r_0}{L_0}, \quad \left|\frac{\partial k_z}{\partial z}\right| \sim \frac{k_0}{L_0}$$

as well as that

$$\frac{|l|}{r_0^2} \le \frac{k_0}{L_0}.$$

This gives a second condition on r_0, namely,

$$r_0^2 \ge \frac{|l|}{2\pi}\lambda_0 L_0. \tag{7}$$

From Eqs. (6) and (7) in the ordering assumptions, one should choose

$$r_0 = \max\left\{\frac{|l|}{2\pi}\lambda_0, \sqrt{\frac{|l|}{2\pi}\lambda_0 L_0}\right\}, \tag{8}$$

which depends on both the topological charge l and the choice of L_0. At last, it can be written

$$\nabla s = i\left[\boldsymbol{k} + \int_0^z \left(\frac{\partial k_z(r,\varphi,z')}{\partial r}\nabla r + \frac{\partial k_z(r,\varphi,z')}{\partial \varphi}\nabla\varphi\right)\mathrm{d}z'\right]s$$

and the integrals are estimated by

$$\delta\boldsymbol{k} = \int_0^z \left(\frac{\partial k_z(r,\varphi,z')}{\partial r}\nabla r + \frac{\partial k_z(r,\varphi,z')}{\partial \varphi}\nabla\varphi\right)\mathrm{d}z' \sim k_0\frac{|z|}{L_0}.$$

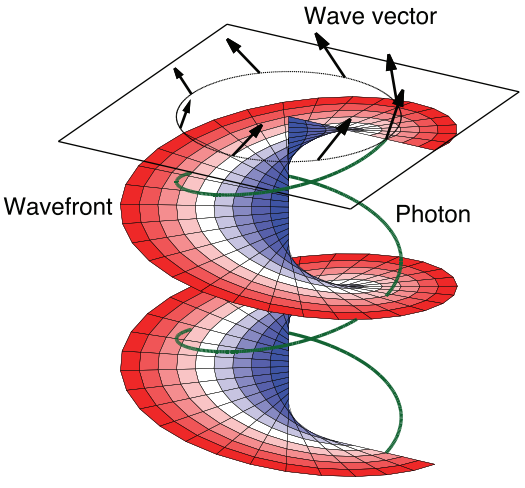

FIG. 1. Schematic diagram of propagation of an optical vortex with a helical wavefront along with a twisted photon with OAM.

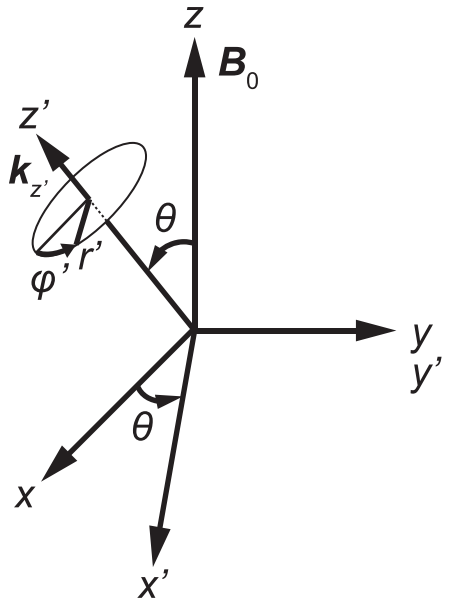

FIG. 2. Coordinate system. The static magnetic field $\boldsymbol{B}_0$ is chosen to be in the z direction. The optical vortex propagates in the z' direction, which lies in the x-z plane.

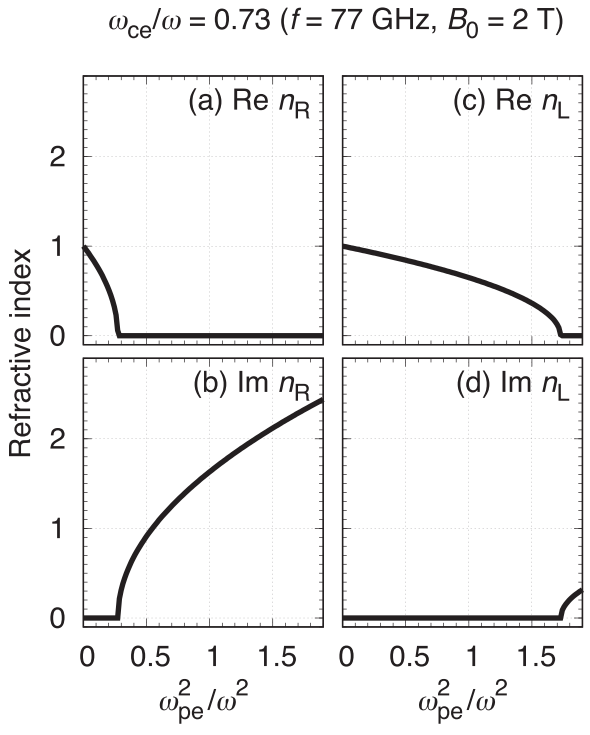

FIG. 3. The z components of the refractive index for (a) and (b) the R wave and (c) and (d) the L wave as a function of ω_{pe}^2/ω^2.

Hence, $\delta\boldsymbol{k}$ can be neglected as compared to $\boldsymbol{k}$ only for a small propagation distance

$$|z| \ll L_0.$$

It should be noted that this is an *ad hoc* assumption introduced here in order to reduce the problem to an algebraic equation rather than a partial differential equation.

Now the contributions to the wave equation can be computed such that

$$\nabla \times \boldsymbol{E} = \frac{1}{2}[\nabla s \times \tilde{\boldsymbol{E}} + s\nabla \times \tilde{\boldsymbol{E}} + \text{c.c.}]$$

and

$$\nabla \times (\nabla \times \boldsymbol{E}) = \frac{1}{2}\left[\{\boldsymbol{k} \otimes \boldsymbol{k} - (\boldsymbol{k}\cdot\boldsymbol{k})\boldsymbol{I}\}\tilde{E}s + O(k_0^2\epsilon) + O\left(k_0^2\frac{|z|}{L_0}\right) + \text{c.c.}\right], \quad (9)$$

where $\boldsymbol{I}$ denotes the identity tensor.

The wave vector given by Eq. (5) denotes the local propagation direction at each position $r\exp[\mathrm{isgn}(l)\varphi]$. The propagation direction of the optical vortex "as a beam" is given by the averaged $\boldsymbol{k}$ on φ from 0 to 2π, i.e.,

$$\boldsymbol{k}_z = \bar{\boldsymbol{k}} \equiv \frac{1}{2\pi}\int_0^{2\pi} \boldsymbol{k}\mathrm{d}\varphi = \left(\frac{1}{2\pi}\int_0^{2\pi} k_z \mathrm{d}\varphi\right)\boldsymbol{e}_z \equiv \bar{k}_z \boldsymbol{e}_z.$$

If the field line of the wave vector $\boldsymbol{k}$ is traced in space, the helical structure appears. In the eikonal approximation, i.e., $E_\sigma \propto \exp[\mathrm{i}S(r,\varphi,z)]$, where $S(\boldsymbol{r})$ expresses the phase front structure expressed as

$$S(\boldsymbol{r}) = -\mathrm{i}|l|\log r + l\varphi + \psi,$$
$$\nabla S(\boldsymbol{r}) \approx \boldsymbol{k} = -\mathrm{i}\frac{|l|}{r}\nabla r + l\nabla\varphi + k_z\nabla z,$$
$$\exp[\mathrm{i}S(\boldsymbol{r})] = r^{|l|}\exp[\mathrm{i}(l\varphi + \psi)].$$

This approximation can be called "vortex optics" as a reference to "geometrical optics" in plane waves. The description of vortex optics can provide a good insight to the propagation properties, but the description is limited under the ordering assumptions. The wave vector $\boldsymbol{k}$ of a plane wave should be in one direction in the Cartesian coordinates. However, the direction of $\boldsymbol{k}$ of the wave with a helical wavefront should be rotated. Ray-tracing can be applied to vortex optics in the same way as geometrical optics. The picture of ray-tracing in vortex optics will match that of a photon rotating around the propagation axis, carrying OAM. Figure 1 shows a schematic

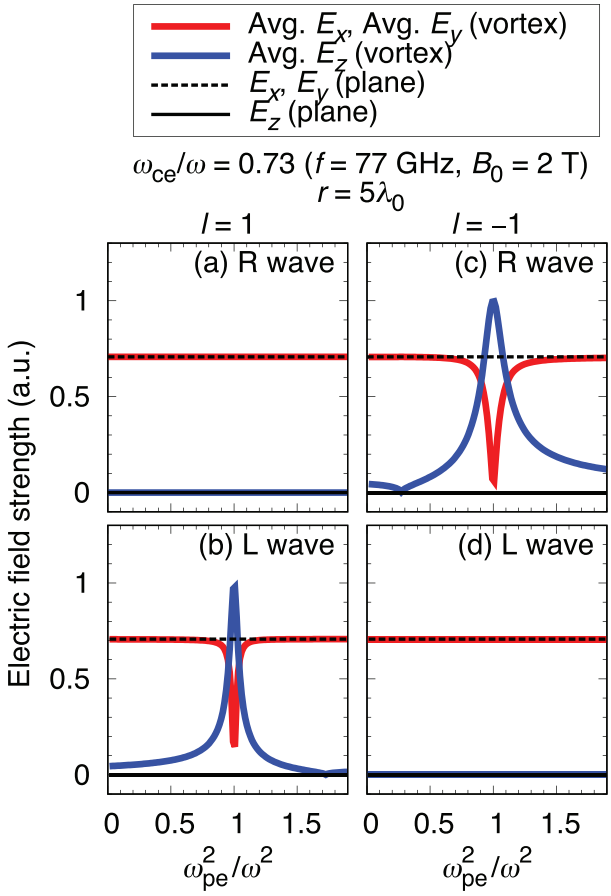

FIG. 4. Electric field strength of each component for (a) and (c) the vortex R waves and (b) and (d) the vortex L waves averaged along φ (see Fig. 5) as a function of ω_{pe}^2/ω^2 in the cases of (a) and (b) $l=1$ and (c) and (d) $l=-1$, respectively, at $r = 5\lambda_0$, and those for the conventional R and L waves of a plane wave for comparison.

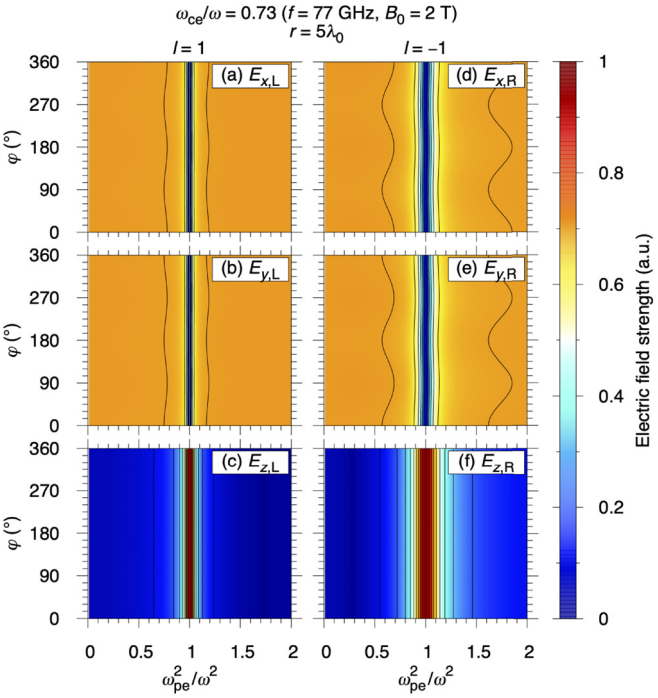

FIG. 5. Electric field strength of each component for [(a)–(c)] the vortex L wave for $l=1$ and [(d)–(f)] the vortex R wave for $l=-1$ as a function of ω_{pe}^2/ω^2 and φ at $r = 5\lambda_0$.

diagram of propagation of the optical vortex. The depicted equiphase plane shows a helical wavefront along with a twisted photon with OAM, in contrast to a flat wavefront of a plane wave without OAM. If the electric field $\boldsymbol{E}$ does not include the amplitude factor $r^{|l|}$, the radial derivative of $\boldsymbol{E}$ is zero under the ordering assumptions. This is not real in the description of optical vortices around the phase singularity. Therefore, the local wave vector $\boldsymbol{k}$ in the eikonal approximation should contain the term in the r direction even if it is imaginary. If the amplitude $\tilde{\boldsymbol{E}}$ is assumed to be slowly varying and the paraxial approximation is applied, the LG beam will be obtained from Eq. (2).

B. Telegraphic equation in cold plasma

The wave field written in Eq. (3) is appropriate to study propagation properties of optical vortices in cold uniform magnetized plasma. Since the plasma has been presumed to be simply uniform and homogeneous in both space and time, the wave electric field is assumed in the Cartesian coordinates system (x, y, z) to be written as

$$\boldsymbol{E} = \frac{1}{2}\left\{\tilde{\boldsymbol{E}}\alpha(r')^{|l|}\exp\left[\mathrm{i}(l\varphi' + \psi' - \omega t)\right] + \text{c.c.}\right\}, \tag{10}$$

where

$$r' = \sqrt{(x')^2 + (y')^2}, \quad \varphi' = \tan^{-1}\frac{y'}{x'},$$

$$\psi' = \int_0^{z'} k_{z'}(r', \varphi', z'')\mathrm{d}z'',$$

$$\begin{pmatrix} x' \\ y' \\ z' \end{pmatrix} = \begin{pmatrix} \cos\theta & 0 & -\sin\theta \\ 0 & 1 & 0 \\ \sin\theta & 0 & \cos\theta \end{pmatrix}\begin{pmatrix} x \\ y \\ z \end{pmatrix}.$$

The coordinate system is defined as shown in Fig. 2. The static magnetic field $\boldsymbol{B}_0$ is directed in the z direction. The optical vortex propagates in the z' direction, which lies in the x-z plane. The propagation angle θ is the angle between $\boldsymbol{B}_0$ and the averaged wave vector

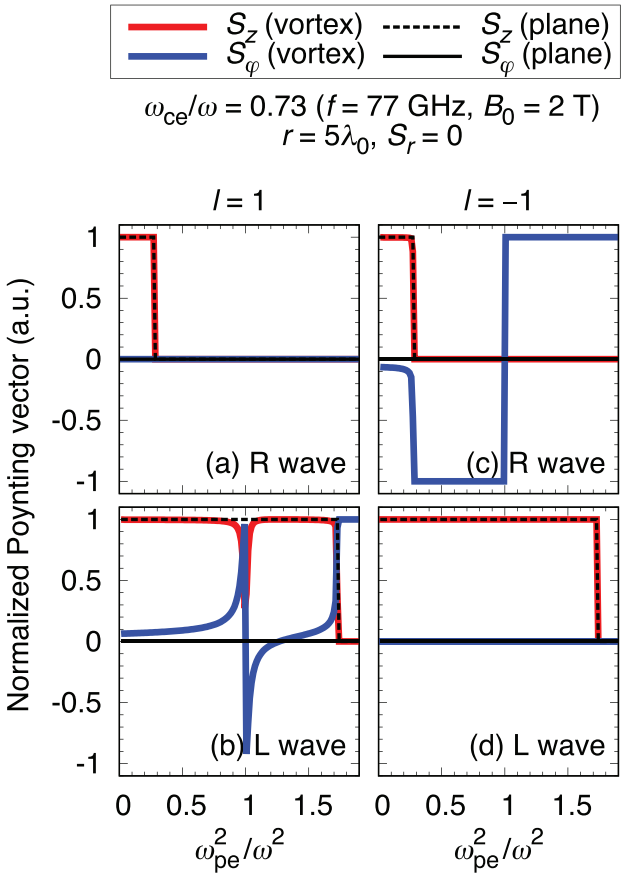

FIG. 6. Poynting vectors for (a) and (c) the vortex R waves and (b) and (d) the vortex L waves as a function of ω_{pe}^2/ω^2 in the cases of (a) and (b) $l = 1$ and (c) and (d) $l = -1$, respectively, at $r = 5\lambda_0$, and those for the conventional R and L waves of a plane wave for comparison. The Poynting vector is normalized by the averaged $|\boldsymbol{S}|$ value along φ from 0 to 2π.

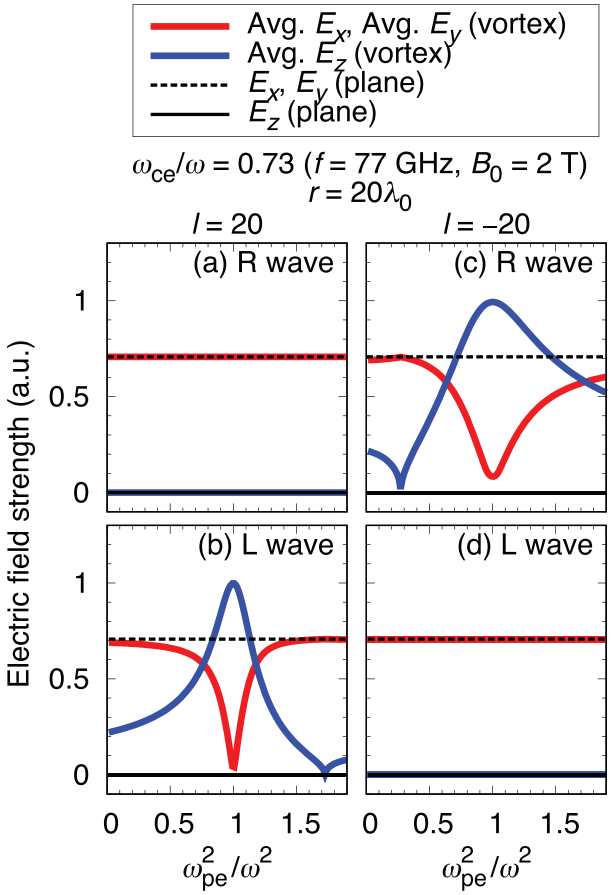

FIG. 7. Electric field strength of each component for (a) and (c) the vortex R waves and (b) and (d) the vortex L waves averaged along φ (see Fig. 8) as a function of ω_{pe}^2/ω^2 in the cases of (a) and (b) $l = 20$ and (c) and (d) $l = -20$, respectively, at $r = 20\lambda_0$, and those for the conventional R and L waves of a plane wave for comparison.

$\bar{\boldsymbol{k}} = \bar{k}_{z'}\boldsymbol{e}_{z'}$, where the wave vector is redefined in the coordinate system as

$$\begin{aligned}\boldsymbol{k} &= \boldsymbol{k}_{r'} + \boldsymbol{k}_{\varphi'} + \boldsymbol{k}_{z'},\\ \boldsymbol{k}_{r'} &= -\mathrm{i}\frac{|l|}{r'}(\cos\varphi'\cos\theta,\ \sin\varphi',\ -\cos\varphi'\sin\theta),\\ \boldsymbol{k}_{\varphi'} &= \frac{l}{r'}(-\sin\varphi'\cos\theta,\ \cos\varphi',\ \sin\varphi'\sin\theta),\\ \boldsymbol{k}_{z'} &= (k_{z'}\sin\theta,\ 0,\ k_{z'}\cos\theta),\\ \bar{k}_{z'} &= \frac{1}{2\pi}\int_0^{2\pi} k_{z'}\,\mathrm{d}\varphi'.\end{aligned}$$

The wave field can also have a parallel component to the propagation direction z' even in the vacuum although a plane wave is a transverse wave without a parallel component to the propagation direction.

Since the linear form of the equation of motion is the same as that in the case of a plane wave,[1,13] the cold plasma dielectric tensor is given by

$$\boldsymbol{\varepsilon}_r(\omega) = \begin{pmatrix} S(\omega) & -\mathrm{i}D(\omega) & 0\\ \mathrm{i}D(\omega) & S(\omega) & 0\\ 0 & 0 & P(\omega)\end{pmatrix},\quad \boldsymbol{\varepsilon}_r^*(-\omega) = \boldsymbol{\varepsilon}_r(\omega), \tag{11}$$

where the dielectric tensor elements S, D, and P are the same notation of Stix.[1,13]

Then, using Eq. (9), the telegraphic equation (2) can be written in the Cartesian coordinates as

$$\frac{1}{2}\left[\boldsymbol{\Lambda}(\omega,\boldsymbol{k})\cdot\tilde{\boldsymbol{E}}s' + \boldsymbol{\Lambda}^*(-\omega,\boldsymbol{k})\cdot\tilde{\boldsymbol{E}}^*(s')^*\right] = \boldsymbol{0}, \tag{12}$$

where

$$\begin{aligned}\boldsymbol{\Lambda}(\omega,\boldsymbol{k}) &\equiv \boldsymbol{k}\otimes\boldsymbol{k} - (\boldsymbol{k}\cdot\boldsymbol{k})\boldsymbol{I} + k_0^2\boldsymbol{\varepsilon}_r(\omega),\\ s' &\equiv \alpha(r')^{|l|}\exp\left[\mathrm{i}(l\varphi' + \psi' - \omega t)\right].\end{aligned}$$

The tensor $\boldsymbol{\Lambda}$ is the standard cold-plasma tensor evaluated at the complex wave vector $\boldsymbol{k}$. The first two terms of the tensor $\boldsymbol{\Lambda}$ are symmetric but $\boldsymbol{\Lambda}$ is not a Hermitian tensor. This characteristic is caused by the complex $\boldsymbol{k}$. Therefore, the helical wavefront structure is expected to produce different propagation properties in comparison to a plane wave. It is also important to notice that Eq. (12) does not simply account for dispersion, but it also includes diffraction effects, as shown in Appendix A. Since $\boldsymbol{\Lambda}$ is not a Hermitian tensor, the eigenvalues are not always real numbers and the eigenvectors are not always orthogonal to each other. The determinant of each coefficient matrix of Eq. (12) should be zero in order to have a non-trivial solution. By using $\boldsymbol{n} = (c/\omega)\boldsymbol{k}$, where $\boldsymbol{n}$ is the refractive index,

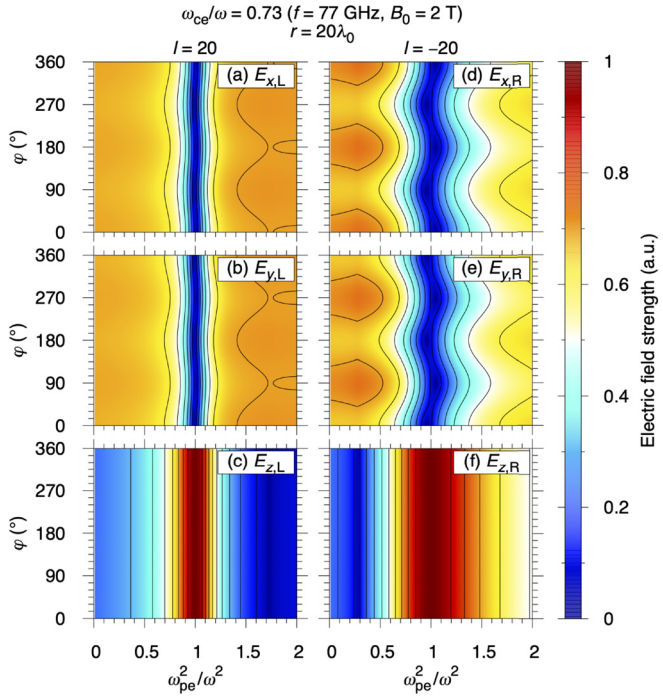

FIG. 8. Electric field strength of each component for [(a)–(c)] the vortex L wave for $l = 20$ and [(d)–(f)] the vortex R wave for $l = -20$ as a function of ω_{pe}^2/ω^2 and φ at $r = 20\lambda_0$.

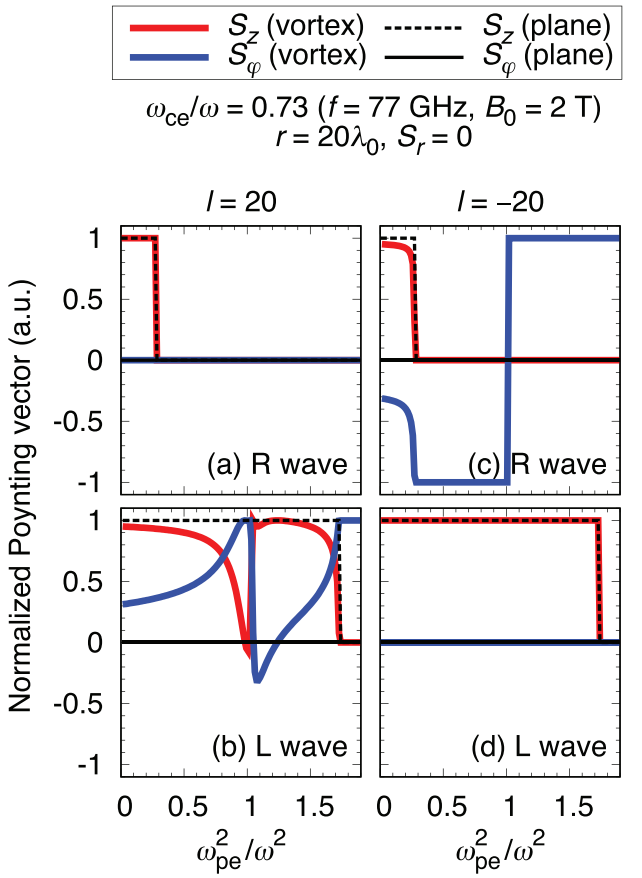

FIG. 9. Poynting vectors for (a) and (c) the vortex R waves and (b) and (d) the vortex L waves as a function of ω_{pe}^2/ω^2 in the cases of (a) and (b) $l = 20$ and (c) and (d) $l = -20$, respectively, at $r = 20\lambda_0$, and those for the conventional R and L waves of a plane wave for comparison. The Poynting vector is normalized by the averaged $|\boldsymbol{S}|$ value along φ from 0 to 2π.

$$\det[\boldsymbol{n}\otimes\boldsymbol{n}-(\boldsymbol{n}\cdot\boldsymbol{n})\boldsymbol{I}+\boldsymbol{\varepsilon}_r]=0 \tag{13}$$

expresses the solvability condition for Eq. (12). With the complex wave vector $\boldsymbol{k}$ under the ordering assumptions, Eq. (13) can be treated simply as an algebraic equation. When the wave is a plane wave, i.e., $l=0$, Eq. (13) is reduced to the dispersion relation with a plane wave.

The Poynting vector of a monochromatic electromagnetic wave with complex $\boldsymbol{n}$ is written as

$$\begin{aligned}\boldsymbol{S}&=\frac{1}{\mu_0}\overline{\boldsymbol{E}\times\boldsymbol{B}}\\&\approx\frac{1}{4c\mu_0}\left\{|\tilde{\boldsymbol{E}}|^2(\boldsymbol{n}+\boldsymbol{n}^*)-(\tilde{\boldsymbol{E}}^*\cdot\boldsymbol{n})\tilde{\boldsymbol{E}}-(\tilde{\boldsymbol{E}}\cdot\boldsymbol{n}^*)\tilde{\boldsymbol{E}}^*\right\}\\&\quad\times|\alpha|^2(r')^{2|l|}\mathrm{e}^{-2\mathrm{Im}\psi'}.\end{aligned} \tag{14}$$

Here, $\overline{\boldsymbol{E}\times\boldsymbol{B}}$ means that the second harmonic oscillating terms are annihilated by the time average. In other words, $\boldsymbol{S}$ is evaluated in the average over a period in time. The derivation is shown in Appendix B. Divergence of the Poynting vector gives the source or the sink of the electromagnetic wave energy, which is written as

$$\nabla\cdot\boldsymbol{S}\approx-k_0^2\frac{|\alpha|^2(r')^{2|l|}\mathrm{e}^{-2\mathrm{Im}\psi'}}{2\mu_0\omega}\tilde{\boldsymbol{E}}^*\cdot\boldsymbol{\varepsilon}_r^a\cdot\tilde{\boldsymbol{E}}=0,$$

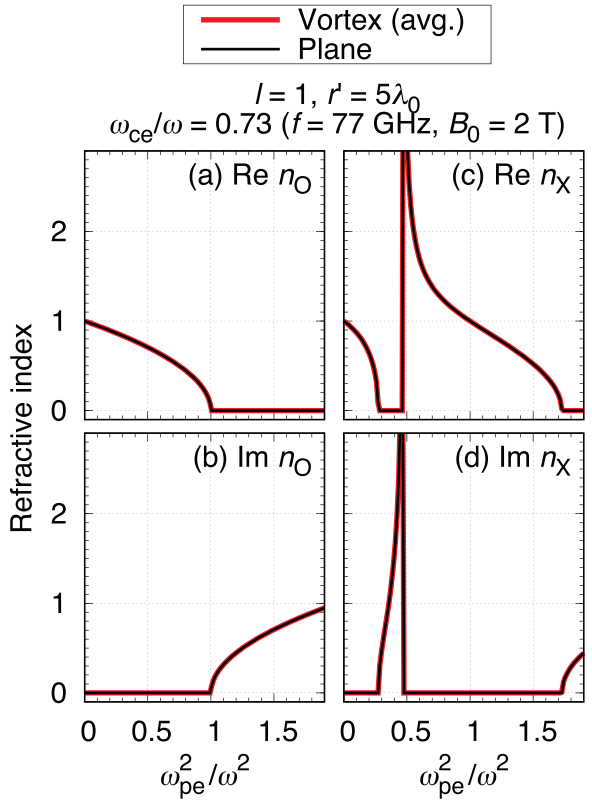

FIG. 10. The z' components of the refractive index for (a) and (b) the vortex O mode and (c) and (d) the vortex X mode averaged along φ' (see Fig. 11) as a function of ω_{pe}^2/ω^2 in the case of $l=1$ at $r'=5\lambda_0$, and those for the conventional O and X modes of a plane wave for comparison.

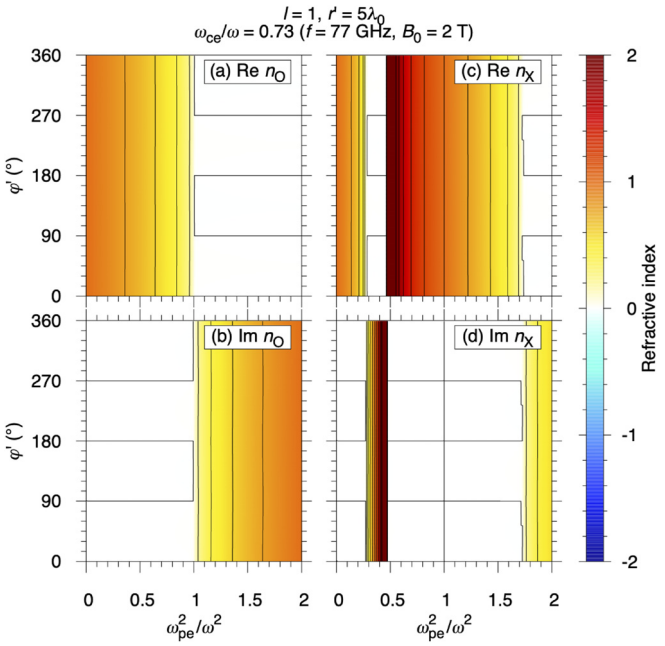

FIG. 11. The z' components of the refractive index for (a) and (b) the vortex O mode and (c) and (d) the vortex X mode as a function of ω_{pe}^2/ω^2 and φ' in the case of $l=1$ at $r'=5\lambda_0$. The refractive index larger/smaller than 2/–2 is colored the same as 2/–2.

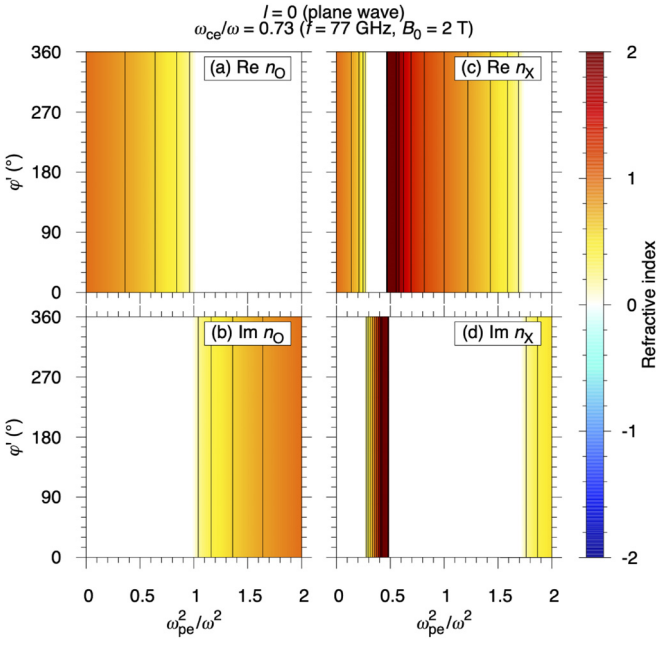

FIG. 12. The z' components of the refractive index for (a) and (b) the conventional O mode and (c) and (d) the conventional X mode of a plane wave as a function of ω_{pe}^2/ω^2 and φ'. The refractive index larger/smaller than 2/–2 is colored the same as 2/–2.

where the last equality holds for a loss-less medium ($\boldsymbol{\varepsilon}_r^a = \mathbf{0}$). The derivation is also shown in Appendix B. This equation shows that the electromagnetic wave energy is conserved when $\boldsymbol{\varepsilon}_r$ is Hermitian. This energy conservation is satisfied even if $\boldsymbol{n}$ is complex due to the helical wavefront structure.

C. Parallel propagation

Two special cases are discussed in more detail in the following: (i) parallel propagation and (ii) perpendicular propagation. First, in the case of parallel propagation, i.e., $\theta = 0$, the solvability condition Eq. (13) becomes

$$\det\begin{pmatrix} S - n_z^2 - n_l^2 & -iD - \mathrm{isgn}(l)n_l^2 & -in_l n_z \\ iD - \mathrm{isgn}(l)n_l^2 & S - n_z^2 + n_l^2 & \mathrm{sgn}(l)n_l n_z \\ -in_l n_z & \mathrm{sgn}(l)n_l n_z & P \end{pmatrix} = 0,$$

where

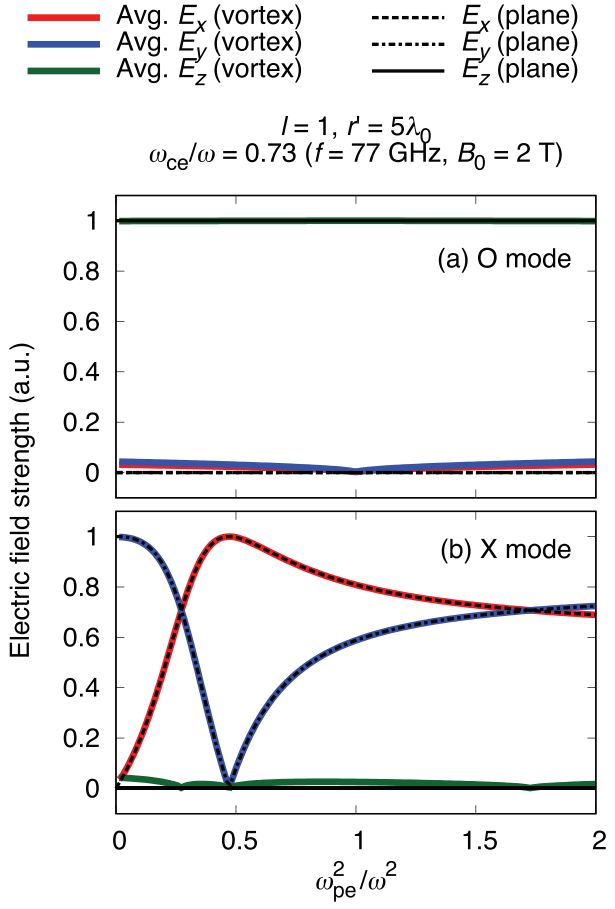

FIG. 13. Electric field strength of each component for (a) the vortex O mode and (b) the vortex X mode averaged along φ' (see Fig. 14) as a function of ω_{pe}^2/ω^2 in the case of $l = 1$ at $r' = 5\lambda_0$, and those for the conventional O and X modes of a plane wave for comparison.

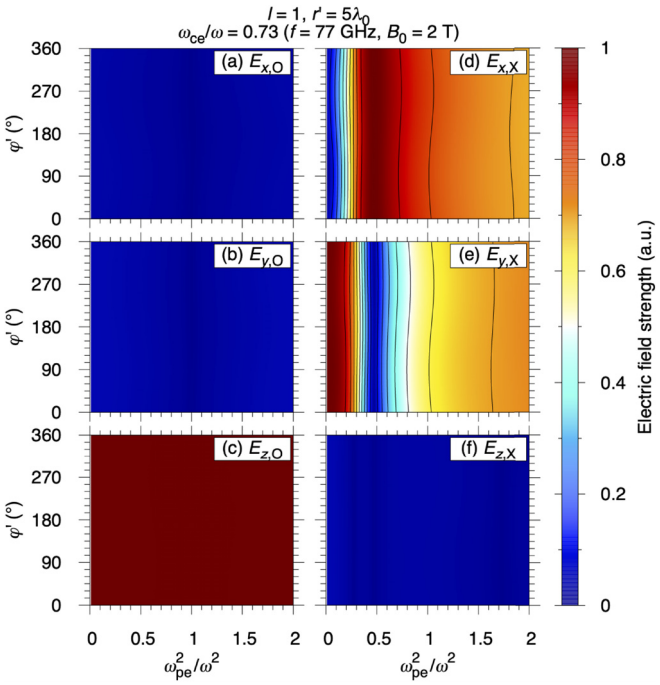

FIG. 14. Electric field strength of each component for [(a)–(c)] the vortex O mode and [(d)–(f)] the vortex X mode as a function of ω_{pe}^2/ω^2 and φ' in the case of $l = 1$ at $r' = 5\lambda_0$.

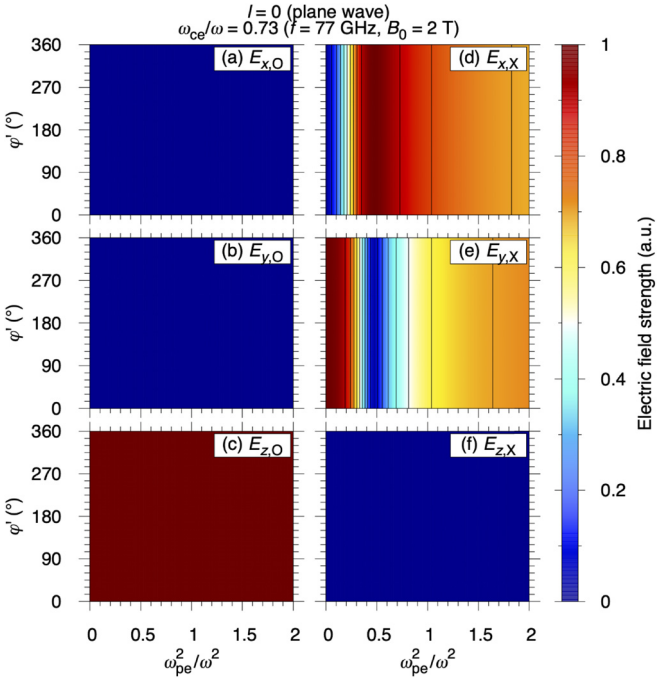

FIG. 15. Electric field strength of each component for [(a)–(c)] the conventional O mode and [(d)–(f)] the conventional X mode of a plane wave as a function of ω_{pe}^2/ω^2 and φ'.

$$n_l \equiv \frac{c}{\omega}\frac{|l|}{r' e^{\mathrm{isgn}(l)\varphi'}}, \quad r' = r = \sqrt{x^2+y^2}, \quad \varphi' = \varphi = \tan^{-1}\frac{y}{x}.$$

The refractive index $n_{z'} = n_z$ can be obtained as

$$(n_z^2 - R)(n_z^2 - L) = 0,$$
$$\therefore n_z^2 = R\,(\equiv S + D), \quad L\,(\equiv S - D),$$

which are the eigenmodes for the so-called right-handed or the so-called left-handed circularly polarized waves (R or L waves) in the magnetized plasma. Figure 3 shows an example of the z components of the refractive index for the R wave and the L wave as a function of $\omega_{pe}^2/\omega^2 \propto n_e$, where ω_{pe} and n_e denote the angular plasma frequency for electrons and the electron density. In these calculations, the static magnetic field strength B_0 is set 2 T for $f = 77$ GHz,[14] thus $\omega_{ce}/\omega = 0.73$, where ω_{ce} denotes the angular EC frequency. The z components of the refractive index are the same as in the case of a plane wave.

However, resultant electric field polarizations are different as follows. In the case of the "vortex" R wave, $n_z^2 \equiv n_R^2 = R$, the electric field components are

$$\tilde{\boldsymbol{E}}_R = [1,\ \mathrm{i},\ 0]\tilde{E}_x \quad (l \geq 0),$$
$$\tilde{\boldsymbol{E}}_R = \left[1,\ \mathrm{i}\frac{PD + n_l^2(P - n_R^2)}{PD - n_l^2(P - n_R^2)},\quad 2\mathrm{i}\frac{n_l n_R D}{PD - n_l^2(P - n_R^2)}\right]\tilde{E}_x \quad (l < 0)$$

while in the case of the vortex L wave, $n_z^2 \equiv n_L^2 = L$, the electric field components are

$$\tilde{\boldsymbol{E}}_L = \left[1,\ -\mathrm{i}\frac{PD - n_l^2(P - n_L^2)}{PD + n_l^2(P - n_L^2)},\quad 2\mathrm{i}\frac{n_l n_L D}{PD + n_l^2(P - n_L^2)}\right]\tilde{E}_x \quad (l \geq 0),$$
$$\tilde{\boldsymbol{E}}_L = [1,\ -\mathrm{i},\ 0]\tilde{E}_x \quad (l < 0).$$

Here, $\tilde{E}_x$ is the amplitude but it is not determined only from Eq. (12). The amplitude can be determined with a boundary condition such as a launching antenna where the electric field is excited. Both waves satisfy

$$\nabla \cdot \boldsymbol{D} \approx \frac{1}{2}\left[\mathrm{i}\boldsymbol{k} \cdot \{\varepsilon_0 \boldsymbol{\varepsilon}_r(\omega) \cdot \tilde{\boldsymbol{E}} s\} - \mathrm{i}\boldsymbol{k}^* \cdot \{\varepsilon_0 \boldsymbol{\varepsilon}_r^*(-\omega) \cdot \tilde{\boldsymbol{E}}^* s^*\}\right] = 0,$$

although $\tilde{\boldsymbol{E}}_R \cdot \tilde{\boldsymbol{E}}_L^* \neq 0$. For the right-handed optical vortex with $l > 0$, the vortex R wave is the pure R wave, but the vortex L wave has a parallel component and is not a left-handed circular polarization, which is different from the pure L wave. For the left-handed optical vortex with $l < 0$, the vortex L wave is the pure L wave, but the vortex R wave has a parallel component and is not a right-handed circular polarization, which is different from the pure R wave. Thus, the polarization of the vortex waves should be expressed in 3D.

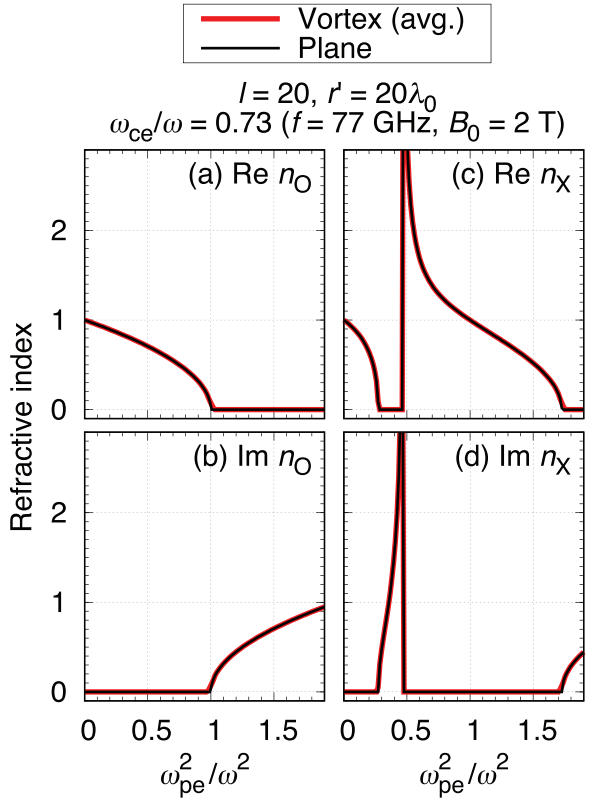

FIG. 16. The z' components of the refractive index for [(a) and (b)] the vortex O mode and [(c) and (d)] the vortex X mode averaged along φ' (see Fig. 17) as a function of ω_{pe}^2/ω^2 in the case of $l = 20$ at $r' = 20\lambda_0$, and those for the conventional O and X modes of a plane wave for comparison.

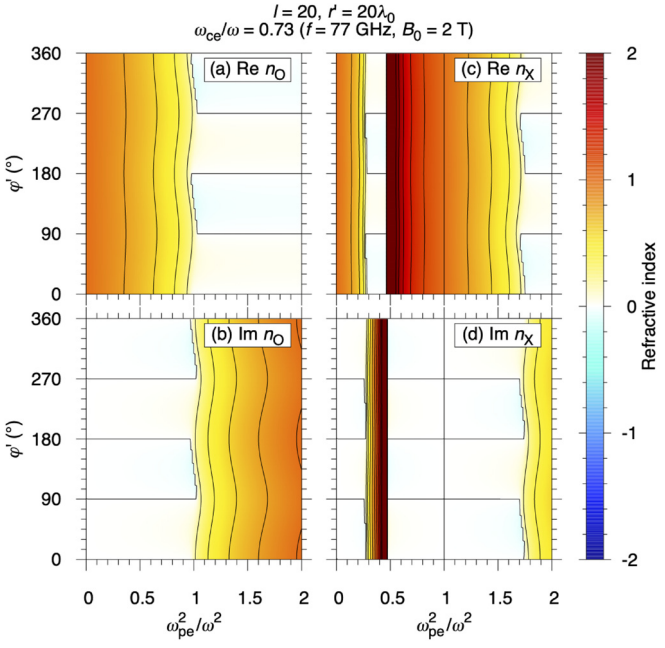

FIG. 17. The z' components of the refractive index for [(a) and (b)] the vortex O mode and [(c) and (d)] the vortex X mode as a function of ω_{pe}^2/ω^2 and φ' in the case of $l = 20$ at $r' = 20\lambda_0$. The refractive index larger/smaller than 2/–2 is colored the same as 2/–2.

The property of energy flux conservation in cold uniform magnetized loss-free plasma can be found in plots of $\boldsymbol{S}$ in Eq. (14). Figure 4 shows the electric field strength of each component for the vortex R waves and the vortex L waves averaged on φ as a function of ω_{pe}^2/ω^2 in the cases of $l=1$ and $l=-1$, respectively, at $r=5\lambda_0$. Each electric field component of a plane wave is also shown for comparison. The dependence of each electric field component on φ is shown in Fig. 5. The Poynting vectors as a function of ω_{pe}^2/ω^2 in these cases are shown in Fig. 6. Here, the scale length L_0 is chosen to be $L_0=100\lambda_0$, which satisfies the validity conditions given by Eqs. (4) and (8). The chosen scale length is applied to following results as well. The averaging operation on φ for the electric field strength and the Poynting vector is considered to be worth performing because a photon rotates around the propagation axis, carrying OAM, in a classical point of view, as shown in Fig. 1. In parallel propagation, the Poynting vector is axisymmetric around the propagation axis, i.e., no dependence on φ, although the electric field is not axisymmetric. The L wave with positive l and the R wave with negative l are not pure circular polarization due to finite values of their parallel components. Because of the dependence of E_z on P, in particular, the parallel components are prominent at the plasma cutoff where $P=0$. The calculated Poynting vector shows the exchange of the energy flux between S_z and S_φ according to the proportion of the parallel component under the energy conservation in the propagation region where $\mathrm{Im}n_{z'}=\mathrm{Im}n_z=0$. The φ component S_φ means the rotating energy flux along the helical wavefront. It is noted that $S_r=0$ is satisfied, so that the energy flux is neither dissipative nor radially diffusive under $\nabla\cdot\boldsymbol{S}\approx 0$. These properties are maintained with increased l/r.

Interestingly for the vortex L wave in the case of $l=20$ at $r=20\lambda_0$ [which also satisfies the validity condition given by Eq. (8)], as shown in Figs. 7–9, it is found that a reversal of the S_z direction occurs at the plasma cutoff, where the absolute value of the sum of the latter negative two terms of S_z given by Eq. (14) becomes larger than the positive value of the first term. The wave with $n_z^2=L>0$ propagates forward but the energy flows backward, similar to a backward wave. The reversal area becomes wider with increasing l/r.

D. Perpendicular propagation

Second, in the case of perpendicular propagation, i.e., $\theta=\pi/2$, the solvability condition Eq. (13) becomes

$$\det\begin{pmatrix} S & -iD+\mathrm{sgn}(l)n_l n_x & in_l n_x \\ iD+\mathrm{sgn}(l)n_l n_x & S-n_x^2+n_l^2 & i\mathrm{sgn}(l)n_l^2 \\ in_l n_x & i\mathrm{sgn}(l)n_l^2 & P-n_x^2-n_l^2 \end{pmatrix}=0,$$

where

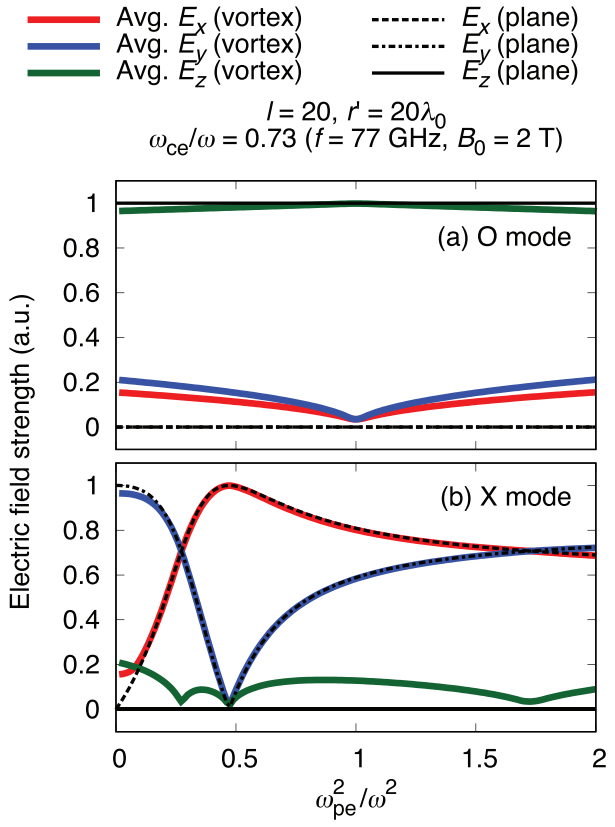

FIG. 18. Electric field strength of each component for (a) the vortex O mode and (b) the vortex X mode averaged along φ' (see Fig. 19) as a function of ω_{pe}^2/ω^2 in the case of $l=20$ at $r'=20\lambda_0$, and those for the conventional O and X modes of a plane wave for comparison.

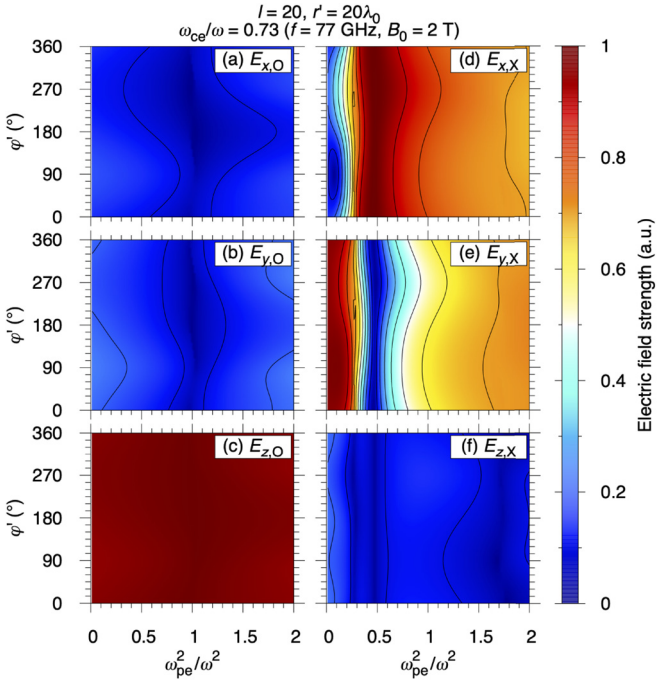

FIG. 19. Electric field strength of each component for [(a)–(c)] the vortex O mode and [(d)–(f)] the vortex X mode as a function of ω_{pe}^2/ω^2 and φ' in the case of $l=20$ at $r'=20\lambda_0$.

$$n_l \equiv \frac{c}{\omega}\frac{|l|}{r' e^{\mathrm{isgn}(l)\varphi'}}, \quad r' = \sqrt{y^2+z^2}, \quad \varphi' = \tan^{-1}\frac{y}{-z}.$$

The refractive index $n_{z'} = n_x$ can be obtained as

$$\begin{aligned} n_x^4 + \alpha n_x^2 + \beta &= 0, \\ \alpha &\equiv -\left(P + \frac{RL}{S}\right) - n_l^2\left(\frac{P}{S} - 1\right), \\ \beta &\equiv \frac{PRL}{S} + n_l^2\left(P - \frac{RL}{S}\right), \\ \therefore n_x^2 &= \frac{1}{2}\left(-\alpha \pm \sqrt{\alpha^2 - 4\beta}\right), \end{aligned} \tag{15}$$

where the terms related to n_l are additions to the refractive indices with a plane wave. The two eigenmodes can be called the vortex ordinary (O) mode and the vortex extraordinary (X) mode. The eigenmodes are reduced to the conventional O and X modes when the terms related to n_l vanishes, i.e., $l = 0$ or $r' \to \infty$, so that these refractive indices depending on n_l are noticeable in the optical vortex with a large topological charge around the propagation axis. The z components of the refractive index for parallel propagation do not depend on n_l because the direction of the wave vector $\boldsymbol{k}$ in relation to $\boldsymbol{B}_0$ is axisymmetric around the propagation axis. On the other hand, the z' components of the refractive index for perpendicular propagation are modulated with φ' since the direction of $\boldsymbol{k}$ in relation to $\boldsymbol{B}_0$ changes with φ' around the propagation axis. That is why the electric field formulation in Eq. (3) is started with k_z, assumed to be a function of r and φ. The relations of electric field components to calculate the polarization are given by

$$\begin{aligned} \tilde{E}_x &= \frac{1}{S}\left\{\mathrm{i}D - \mathrm{sgn}(l)n_l n_\sigma\right\}\tilde{E}_y - \mathrm{i}\frac{n_l n_\sigma}{S}\tilde{E}_z, \\ \tilde{E}_z &= \frac{(D^2 + n_l^2 n_\sigma^2) - S(S - n_\sigma^2 + n_l^2)}{n_l\left\{Dn_\sigma - \mathrm{isgn}(l)n_l n_\sigma^2 + \mathrm{isgn}(l)n_l S\right\}}\tilde{E}_y, \\ &(\sigma = \mathrm{O}, \mathrm{X}), \end{aligned} \tag{16}$$

which satisfy $\nabla \cdot \boldsymbol{D} \approx 0$, although $\tilde{\boldsymbol{E}}_\mathrm{O} \cdot \tilde{\boldsymbol{E}}_\mathrm{X}^* \neq 0$.

In order to investigate the propagation properties of the vortex O and X modes, the z' components of the refractive index for the two eigenmodes are calculated for the optical vortices with (i) $l = 1$ at $r' = 5\lambda_0$ and (ii) $l = 20$ at $r' = 20\lambda_0$. Again, the scale length L_0 is chosen to be $L_0 = 100\lambda_0$, so that both cases satisfy the validity conditions given by Eqs. (4) and (8). Figure 10 shows refractive indices for the vortex O mode, $n_{z'} \equiv n_\mathrm{O}$, and the vortex X mode, $n_{z'} \equiv n_\mathrm{X}$, as a function of ω_{pe}^2/ω^2 in the case of $l = 1$ at $r' = 5\lambda_0$. n_O and n_X are averaged along φ' to be compared with the conventional O and X modes of a plane wave. Figure 11 shows n_O and n_X as a function of ω_{pe}^2/ω^2 and φ' in the case of $l = 1$ at $r' = 5\lambda_0$. Figure 12 shows n_O and n_X of a plane wave ($l = 0$) as a function of ω_{pe}^2/ω^2 and φ' as a reference although they do not depend on φ'. Here, for $l \neq 0$, since there are

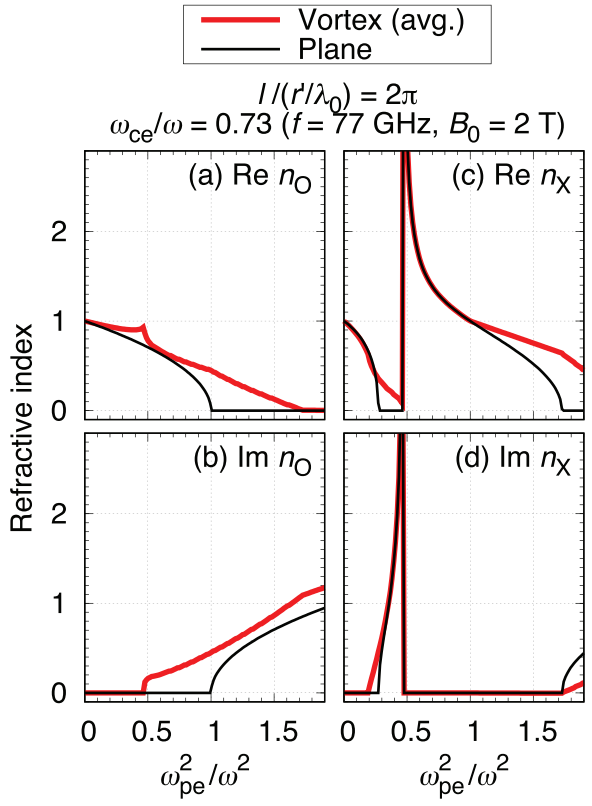

FIG. 20. The z' components of the refractive index for [(a) and (b)] the vortex O mode and [(c) and (d)] the vortex X mode averaged along φ' (see Fig. 21) as a function of ω_{pe}^2/ω^2 in the case of $l/(r'/\lambda_0) = 2\pi$, and those for the conventional O and X modes of a plane wave for comparison.

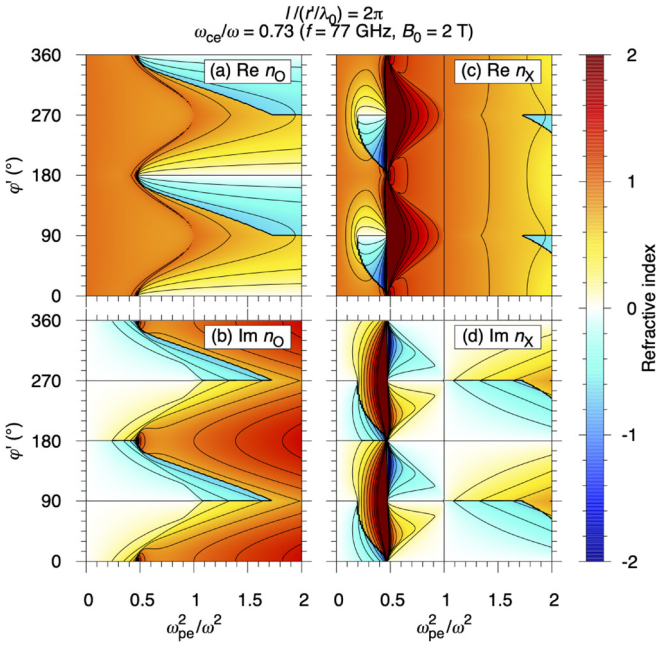

FIG. 21. The z' components of the refractive index for [(a) and (b)] the vortex O mode and [(c) and (d)] the vortex X mode as a function of ω_{pe}^2/ω^2 and φ' in the case of $l/(r'/\lambda_0) = 2\pi$. The refractive index larger/smaller than 2/–2 is colored the same as 2/–2.

two complex conjugate roots of the squared refractive index for each mode ($\sigma = \mathrm{O}, \mathrm{X}$), the sign is chosen in the following ways: (i) The positive imaginary part is chosen for $\mathrm{Re}n_\sigma^2 \leq 0$ so that the imaginary part averaged on φ' with the small real part becomes almost the conventional imaginary part with zero real part in the evanescent region. (ii) The positive real part is chosen for $\mathrm{Re}n_\sigma^2 > 0$ so that the forward propagation can be treated with zero or the small imaginary part. As a result, n_O and n_X in the case of $l = 1$ at $r' = 5\lambda_0$ are almost identical to the conventional n_O and n_X. Figure 13 shows electric field strength of each component for the vortex O mode and the vortex X mode averaged on φ' as a function of $\omega_{\mathrm{pe}}^2/\omega^2$ in the case of $l = 1$ at $r' = 5\lambda_0$. Each electric field component of a plane wave is also shown for comparison. The dependence of each electric field component on φ' in the case of $l = 1$ at $r' = 5\lambda_0$ is shown in Fig. 14. For a reference, the dependence of each electric field component on φ' for a plane wave is also shown in Fig. 15 although the electric field does not depend on φ'. The result indicates that the electric field pattern in the case of $l = 1$ at $r' = 5\lambda_0$ is almost identical to that in the case of a plane wave.

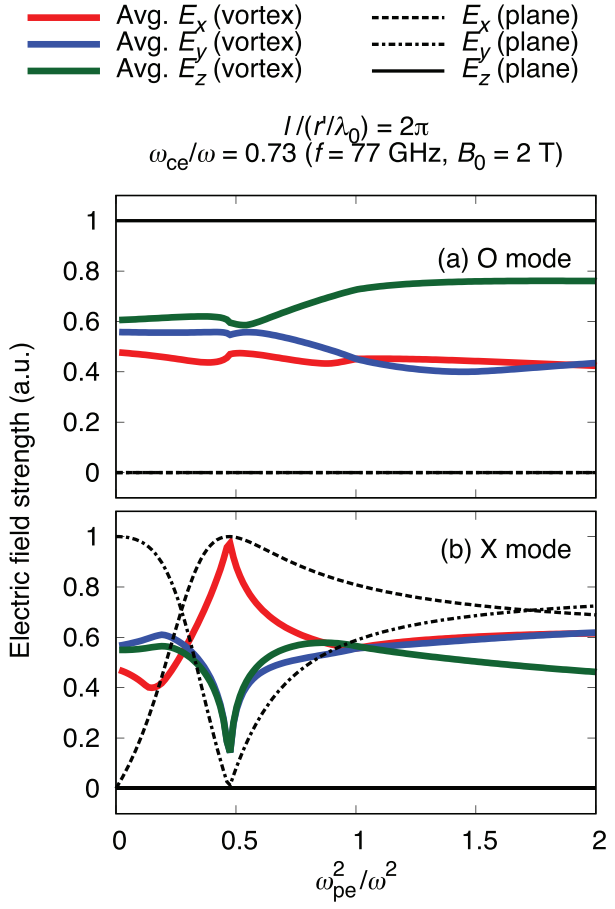

FIG. 22. Electric field strength of each component for (a) the vortex O mode and (b) the vortex X mode averaged along φ' (see Fig. 23) as a function of $\omega_{\mathrm{pe}}^2/\omega^2$ in the case of $l/(r'/\lambda_0) = 2\pi$, and those for the conventional O and X modes of a plane wave for comparison.

Figures 16 and 17 show n_O and n_X in the case of $l = 20$ at $r' = 20\lambda_0$. Those refractive indices n_O and n_X are modulated with φ', but those averaged along φ' are almost identical to the conventional n_O and n_X. Figures 18 and 19 show the electric field strength of each component for the vortex O mode and the vortex X mode in the case of $l = 20$ at $r' = 20\lambda_0$. The z component of the electric field, E_z, parallel to $\boldsymbol{B}_0$ is dominant for the vortex O mode as in the conventional O mode with a plane wave, but the finite strength of the other two components, E_x and E_y, exist in a wide range of n_e. The vortex O mode is not the pure linear polarization directed in $\boldsymbol{B}_0$ and has a component parallel to the propagation direction. Although the conventional O mode is not affected by $\boldsymbol{B}_0$, the vortex O mode is affected by $\boldsymbol{B}_0$ due to the new terms on n_l in Eq. (15) which include S with B_0. It is noted that $P - RL/S = P/S - 1$, thus the terms on n_l are not affected by R and L. This refractive index with the wave with a helical wavefront suggests that the vortex O mode can experience the effect of the upper hybrid resonance (UHR) at $S = 0$ when $n_l \propto |l|/r'$ becomes large. The vortex X mode shows a similar trend to the conventional X mode with a plane wave but has a component parallel to $\boldsymbol{B}_0$. The electric fields for both modes are modulated with φ', but the contribution of the n_l terms to the z' components of the refractive index is too small to change the refractive indices of the vortex O and X modes compared to the conventional modes with a plane wave.

The theory discussed here is valid for r_0 limited by Eq. (8). Under reasonable choices of l and L_0, the element of the first condition $|l|\lambda_0/(2\pi)$ is normally shorter than that of the second condition

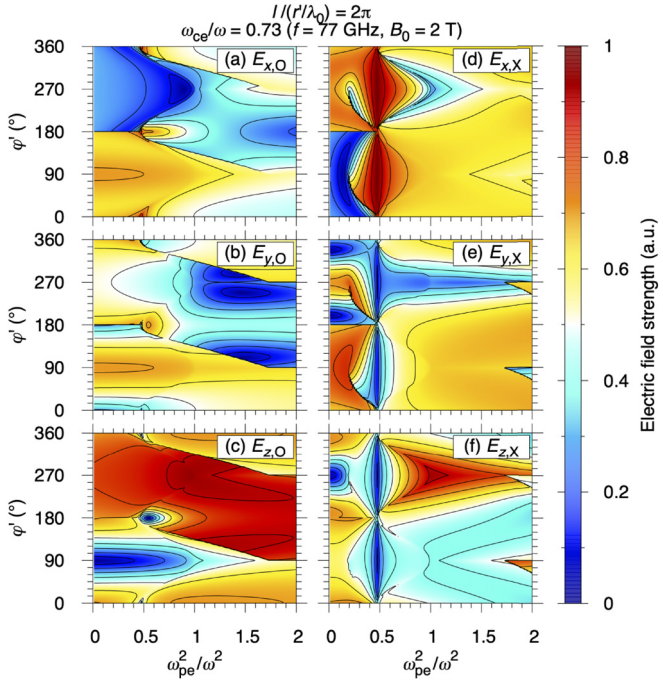

FIG. 23. Electric field strength of each component for [(a)–(c)] the vortex O mode and [(d)–(f)] the vortex X mode as a function of $\omega_{\mathrm{pe}}^2/\omega^2$ and φ' in the case of $l/(r'/\lambda_0) = 2\pi$.

$\sqrt{|l|/(2\pi)}\sqrt{\lambda_0 L_0}$. Thus, in the two cases of $l=1$ and $l=20$ discussed above, r_0 is chosen by the limit of the second element. Aside from how an optical vortex with huge l and a huge beam radius can be generated practically, it is theoretically valuable to investigate the region where the first element is greater than the second element; thus, r_0 is chosen by the limit of the first element. Because n_l is proportional to $|l|/r'$, the effect of the new n_l terms on the refractive indices is most significant when $l/(r'/\lambda_0)=2\pi$. The results of this case are shown in Figs. 20 and 21. The refractive indices n_O and n_X deviate from the conventional indices of a plane wave, strongly modulated with φ'. As suggested by the new terms on n_l, the vortex O mode is influenced by the UHR from the lower n_e side and then seems to become evanescent in the higher n_e side. As in the conventional X mode, the UHR also occurs for the vortex X mode from the higher n_e side and the vortex X mode can propagate in the higher n_e region with the zero imaginary part although the vortex X mode seems to become evanescent between the modified right-hand (R) cutoff and the UHR with the positive imaginary part. Figures 22 and 23 show electric field strength of each component for the vortex O mode and the vortex X mode in the case of $l/(r'/\lambda_0)=2\pi$. The electric field components entirely deviate from the conventional electric field components in a plane wave. Due to the effect of S in the n_l term, not only the electric field of the vortex X mode but also the electric field of the vortex O mode is affected by the UHR, specifically at $\varphi'=0$ and π where $n_l^2=1$. The parallel component E_x is comparable to the other two components even in the vortex O mode. One may expect that the electric fields of both modes become similar to each other around the UHR where n_O also diverges when $|l|/r'$ can be much larger. However, the region where $|l|/(r'/\lambda_0)>2\pi$ is not accessible because the theory discussed here is not valid there. The region may be accessible when the ordering assumptions can be relaxed to treat smaller r_0 and a partial differential equation for a complex-valued phase function $\psi(r',\varphi',z')$ can be solved instead of the algebraic equation (12), which is left for a future article. If the expectation is valid in the more-advanced theory, E_x, parallel to the propagation direction, would become the largest component for both modes with a high wavenumber around the UHR. This unique property of propagation implies that the vortex O mode injected from the lower n_e side can be converted into the vortex X mode at the UHR. In addition, it would be anticipated that the direct conversion from the vortex O mode into the electron Bernstein wave (EBW) partly occurs at the UHR when a finite electron temperature is taken into account. This method is relatively similar to the mode conversion method in which the EBW is excited from the X mode injected perpendicularly from the low

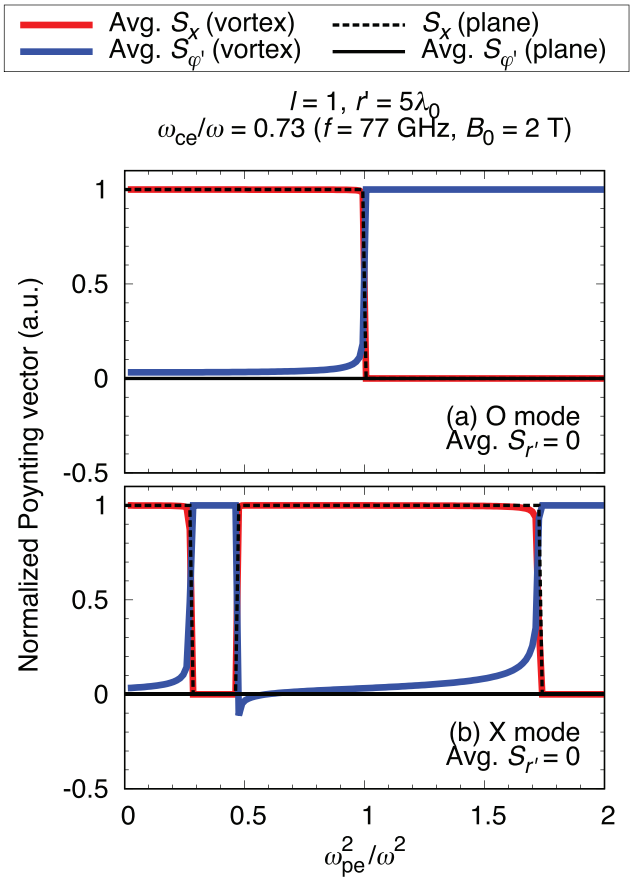

FIG. 24. Poynting vectors for (a) the vortex O mode and (b) the vortex X mode as a function of ω_{pe}^2/ω^2 in the case of $l=1$ at $r'=5\lambda_0$, and those for the conventional O and X modes of a plane wave for comparison. The Poynting vectors are normalized by the averaged $|S|$ value along φ' from 0 to 2π (see Fig. 25).

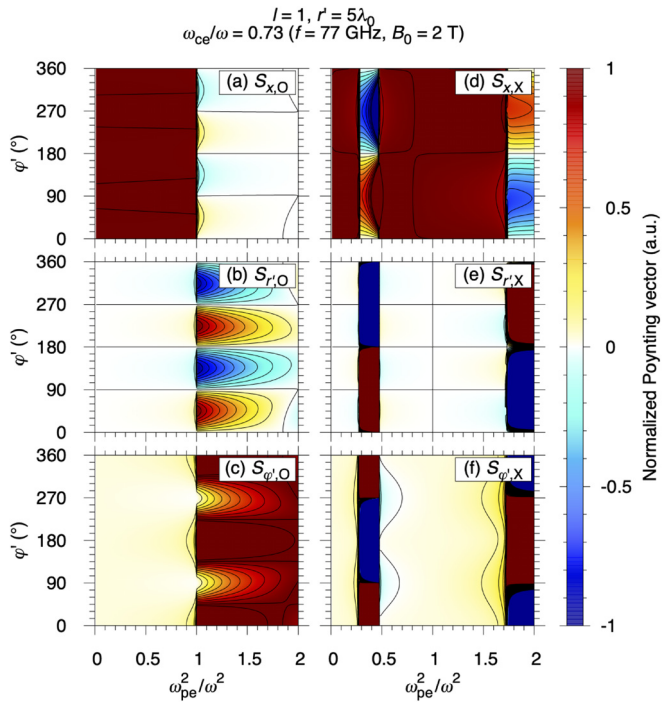

FIG. 25. Poynting vectors for [(a)–(c)] the vortex O mode and [(d)–(f)] the vortex X mode as a function of ω_{pe}^2/ω^2 and φ' in the case of $l=1$ at $r'=5\lambda_0$. The Poynting vectors are normalized by the averaged $|S|$ value along φ' from 0 to 2π.

field side, whose disadvantage is that the X mode should penetrate through the evanescent region. This paper focuses only on the propagation properties in cold plasma under the strong limitation in the ordering assumptions. This new suggestion for the mode conversion should be verified also in a future article.

Contrary to parallel propagation, the refractive index, the electric field, and the Poynting vector in perpendicular propagation are not axisymmetric. However, the property of constant energy flux averaged along φ' can be maintained. Figures 24–29 show the Poynting vectors in the cases of $l=1$ at $r'=5\lambda_0$, $l=20$ at $r'=20\lambda_0$, and ideal $l/(r'/\lambda_0)=2\pi$. For a reference, the dependence of the Poynting vector for a plane wave is also shown in Fig. 30. It is noted that $\nabla\cdot\boldsymbol{S}\approx 0$ is satisfied locally in all three cases. Although the calculated Poynting vector shows the exchange of the energy flux among all three components including $S_{r'}$ under the energy conservation in the propagation region where $\mathrm{Im}n_{z'}=\mathrm{Im}n_x=0$, the averaged $S_{r'}$ along φ' over a period from 0 to 2π becomes zero. Therefore, the property of constant non-dissipative radially-non-diffusive energy flux is maintained under the energy conservation even if $\boldsymbol{n}$ is complex due to the helical wavefront structure. It is anticipated that in increased $|l|/r'$ the energy averagely flows forward along with the rotating energy flux in the plasma beyond the plasma cutoff for the vortex O mode and the left-hand cutoff for the vortex X mode.

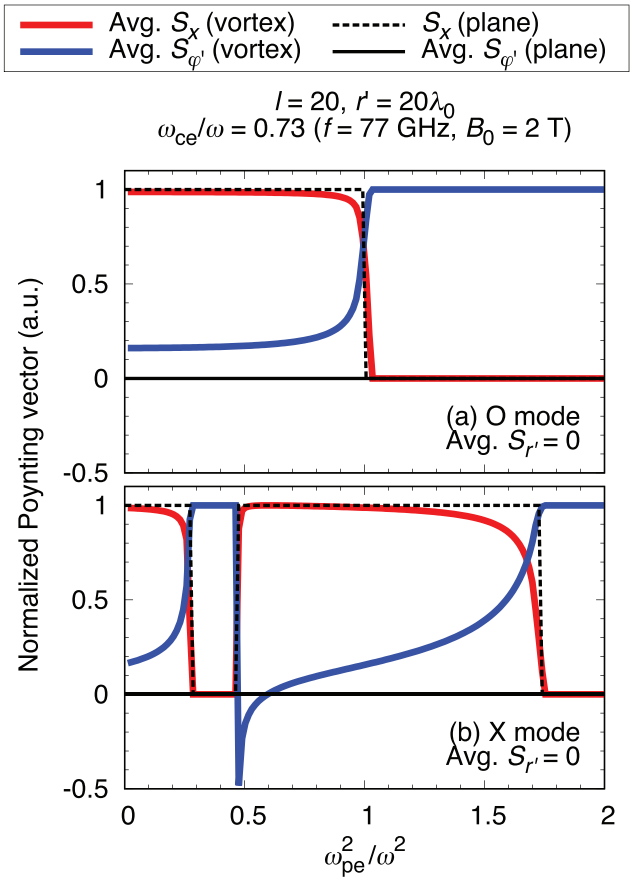

FIG. 26. Poynting vectors for (a) the vortex O mode and (b) the vortex X mode as a function of ω_{pe}^2/ω^2 in the case of $l=20$ at $r'=20\lambda_0$, and those for the conventional O and X modes of a plane wave for comparison. The Poynting vectors are normalized by the averaged $|\boldsymbol{S}|$ value along φ' from 0 to 2π (see Fig. 27).

III. PROPAGATION OF AN EC WAVE WITH A HELICAL WAVEFRONT WITH 3D SIMULATIONS

Propagation properties of an EC wave with a helical wavefront are discussed in Sec. II by using Eq. (10), which is suitable for investigating analytically as has been done with a plane wave. In real situations for practical use, however, the wave amplitude is restricted to a finite beam size. In this section, propagation of LG beams is numerically investigated with 3D simulations by the commercial FEM (finite element method) software, COMSOL Multiphysics with its RF solver.[15–18] The simulation box is limited to a cube with a side length of 20 mm due to computational resources. The size of tetrahedral meshes is 0.3 mm at a maximum and 0.03 mm at a minimum. The wave frequency f is set at 77 GHz. The static magnetic field B_0 is set at 2 T in the z direction. In order to excite the O mode, E_z in a form of the LG beam is excited at the plane of $x=0$, given by

$$E_z(x,y,z)=E_0\left(\frac{r^2}{w^2(x)}\right)^{|l|}\frac{w_0}{w(x)}\times\exp\left[-\frac{r^2}{w(x)^2}+\mathrm{i}\left\{-k_0\frac{r^2}{2R(x)}-l\varphi+(|l|+1)\zeta(x)\right\}\right]\quad\text{at}\quad x=0, \tag{17}$$

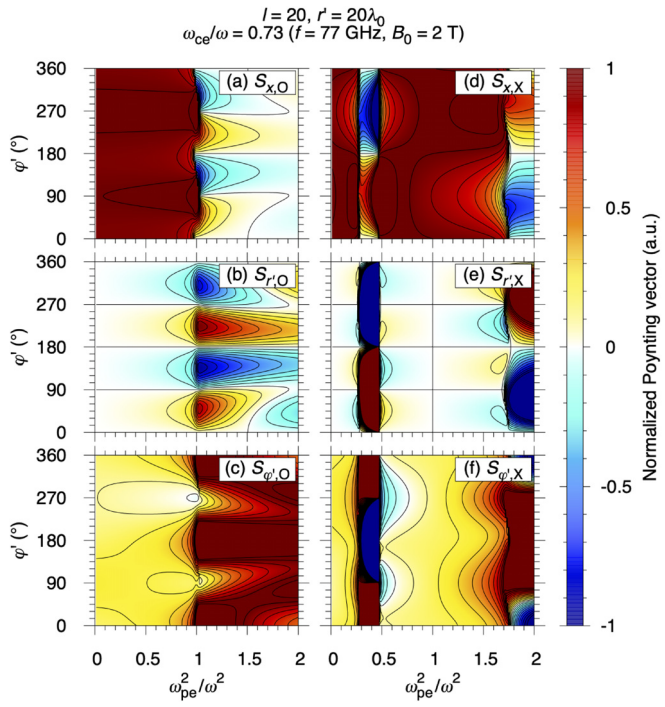

FIG. 27. Poynting vectors for [(a)–(c)] the vortex O mode and [(d)–(f)] the vortex X mode as a function of ω_{pe}^2/ω^2 and φ' in the case of $l=20$ at $r'=20\lambda_0$. The Poynting vectors are normalized by the averaged $|\boldsymbol{S}|$ value along φ' from 0 to 2π.

where

$$r^2 = y^2 + z^2, \quad \varphi = \tan^{-1}\frac{y}{-z},$$
$$w(x) = w_0\sqrt{1 + \left(\frac{x - x_R}{x_R}\right)^2}, \quad x_R = \frac{\pi w_0^2}{\lambda_0},$$
$$R(x) = (x - x_R)\left\{1 + \left(\frac{x_R}{x - x_R}\right)^2\right\}, \quad \zeta(x) = \tan^{-1}\frac{x - x_R}{x_R}.$$

The focal point x_R is set at 10 mm and the beam waist w_0 becomes 3.5 mm in the vacuum. Propagation of the excited wave in the x direction is calculated by solving the telegraphic equation given by Eq. (2). Here, the cold plasma dielectric tensor $\boldsymbol{\varepsilon}_r$ given in Eq. (11) includes the effect of collisions[1] with the artificial collision frequency of $\nu_0 = 0.01\omega$. The specific number of 0.01 is simply an *ad hoc* number in order to prevent numerical divergence at the UHR where resonant waves with high wavenumbers should be collisionally damped. The scattering boundary condition (SBC) is applied to the boundaries of the cube so that waves can pass through the domain boundaries without reflection. The SBC is one of the ready-made functions of the COMSOL RF solver. A numerical test of LG beam propagation is performed in the vacuum condition to be compared with theoretical LG beam propagation. The result shows good agreement with each other.

In order to confirm whether the COMSOL model is correctly constructed, the refractive indices are calculated with COMSOL under constant n_e in the modeling domain. Figure 31 shows the comparison of the theoretical refractive indices calculated from Eq. (15) and those calculated with the COMSOL model in the case of $l = 1$. The refractive index for each COMSOL simulation is obtained by fitting the electric field profile to the LG beam given by Eq. (17). The results indicate that the COMSOL simulations reproduce the theoretical refractive indices in the case of $l = 1$.

Then, propagation of LG beams is calculated under a varied n_e profile. The n_e profile is set to change in the x direction, given by $n_e(x) = n_{e,max}x/L_n$, where $n_{e,max} = 5 \times 10^{19}$ m^{-3} and $L_n = 20$ mm. Thus, the R cutoff layer and the UHR layer exist in the simulation box. The magnetized plasma is uniform in the y and z directions. Figure 32 shows the amplitude distributions of E_z and E_x on the x-y plane at $z = 0$ mm in the case of $l = 0$. The topological charge of $l = 0$ means the conventional Gaussian beam without OAM, which is commonly used for EC heating and current drive in magnetic fusion plasma. The excited linearly polarized E_z parallel to $\boldsymbol{B}_0$ is observed to propagate in the x direction, under the O-mode polarization maintained. The amplitude of E_x is negligible in comparison to that of E_z. Although a

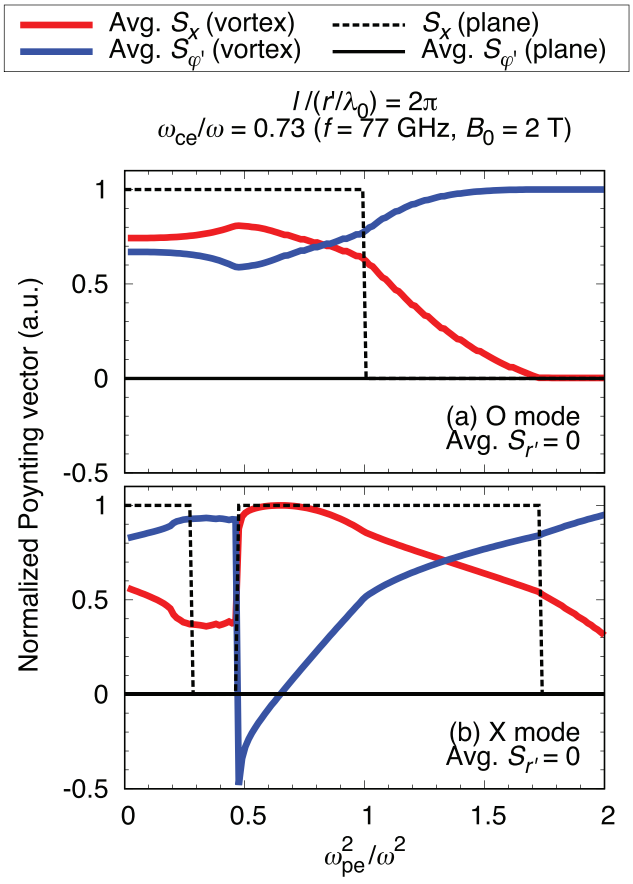

FIG. 28. Poynting vectors for (a) the vortex O mode and (b) the vortex X mode as a function of ω_{pe}^2/ω^2 in the case of $l/(r'/\lambda_0) = 2\pi$, and those for the conventional O and X modes of a plane wave for comparison. The Poynting vectors are normalized by the averaged $|\boldsymbol{S}|$ value along φ' from 0 to 2π (see Fig. 29).

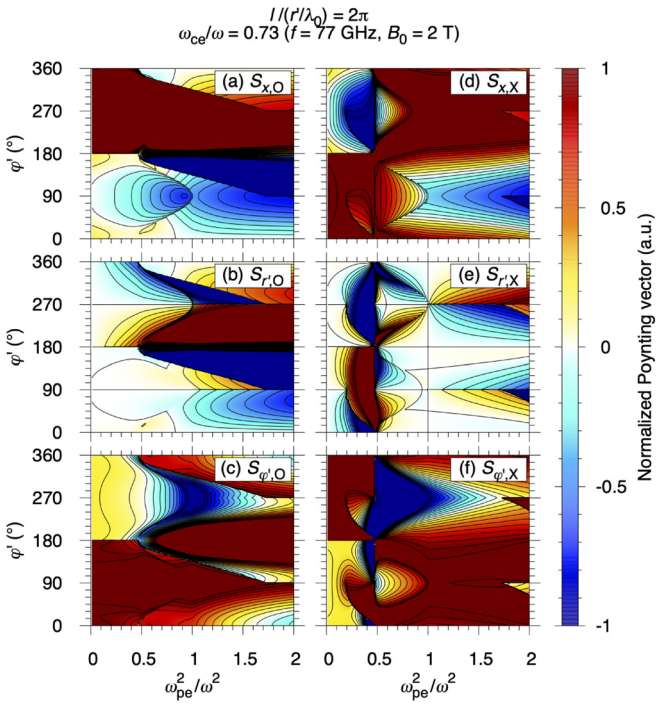

FIG. 29. Poynting vectors for [(a)–(c)] the vortex O mode and [(d)–(f)] the vortex X mode as a function of ω_{pe}^2/ω^2 and φ' in the case of $l/(r'/\lambda_0) = 2\pi$. The Poynting vectors are normalized by the averaged $|\boldsymbol{S}|$ value along φ' from 0 to 2π.

Gaussian beam is excited, a more complicated wave pattern of E_z such as higher-order modes is observed. This pattern is not observed in lower n_e plasma. This cause is not clear yet but the scattered waves by relatively high n_e plasma may be partially reflected at the boundaries. Larger simulation boxes may improve purity of the mode pattern. Figure 33 shows the phase distributions of E_z and E_x on the y-z planes at $x = 0$ mm and $x = 20$ mm. The phase is calculated by $E_\sigma = \tan^{-1}(\mathrm{Im}E_\sigma/\mathrm{Re}E_\sigma)$ for $\sigma = z, x$. The phase distribution of E_z at $x = 0$ mm follows the contours of the function $l\varphi$ mod 2π. Due to zero OAM, the phase of E_z is almost axisymmetric around the propagation axis of $y = z = 0$ mm. The phase distribution of E_x shows discontinuities, e.g., at $z = 0$ mm. Although the amplitude of E_x is negligible compared to that of E_z, finite E_x exists and it seems that the polarity of E_x changes at $z = 0$ mm. However, this phase pattern is not characterized with $l\varphi$ of an optical vortex.

A remarkable phenomenon is observed in the propagation of an EC wave with a helical wavefront in the case of $l = 1$, as shown in Figs. 34 and 35. The excited LG beam E_z with $l = 1$ propagates to the UHR layer with $S = 0$. Then, the beam is observed to diffuse outward over the UHR layer, while E_x parallel to the propagation direction with the wavenumber much higher than that of E_z is observed to be excited and to propagate to the higher n_e region. The amplitude of E_x seems to be larger around the propagation axis, while that of E_z is smaller due to the outward diffusion. This result suggests that a portion of E_z with the O-mode polarization is converted into E_x with the X-mode polarization. The phase distribution of E_x around the propagation axis

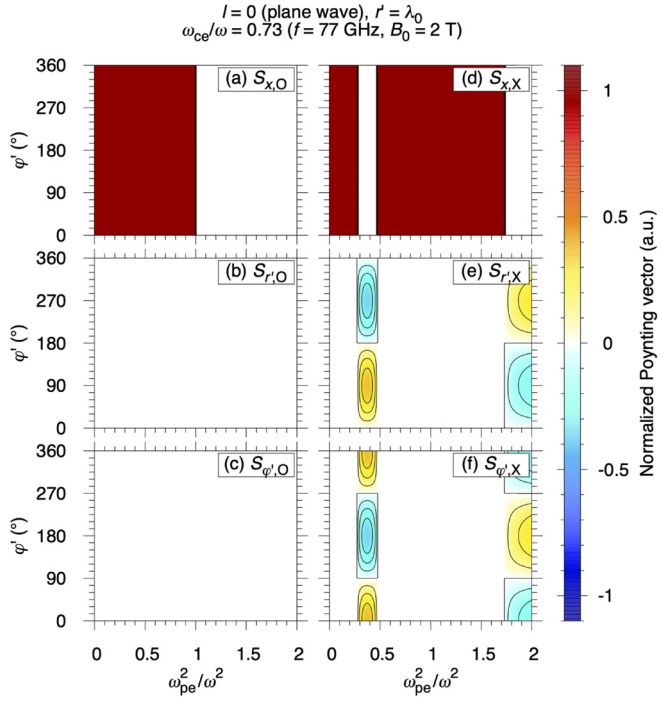

FIG. 30. Poynting vectors for [(a)–(c)] the conventional O mode and [(d)–(f)] the conventional X mode of a plane wave as a function of ω_{pe}^2/ω^2 and φ' under $r' = \lambda_0$. The Poynting vectors are normalized by the averaged $|S|$ value along φ' from 0 to 2π.

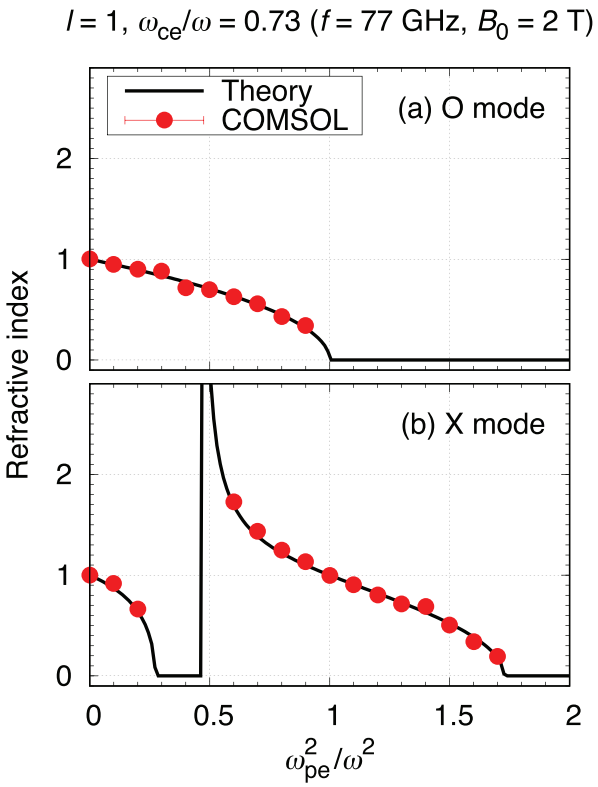

FIG. 31. Refractive indices of (a) the O mode and (b) the X mode calculated from Eq. (15) averaged along φ' in the case of $l = 1$ and $r' = 5\lambda_0$, and those calculated with COMSOL simulations in the case of $w_0 = 3.5$ mm under constant n_e.

with a smaller radius shows the property of $l = 0$, while that of E_z shows the property of $l = 1$, probably because the relation of E_x and E_z shown in Eq. (16) indicates that the topological charge of E_x is one smaller than that of E_z due to the factor of $1/e^{i\varphi}$. The property of $l = 0$ in E_x is recognized in Fig. 34(b), where the amplitude of E_x is similar to a plane wave with high wavenumbers. It is noted that when the LG beam with the X-mode polarization is excited, the X mode is reflected

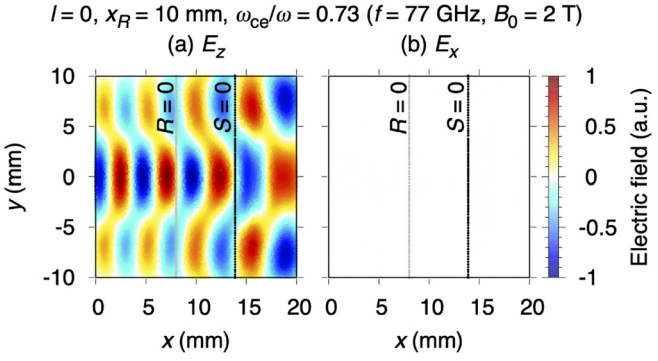

FIG. 32. Amplitude distributions of (a) E_z and (b) E_x on the x-y plane at $z = 0$ mm in the case of $l = 0$.

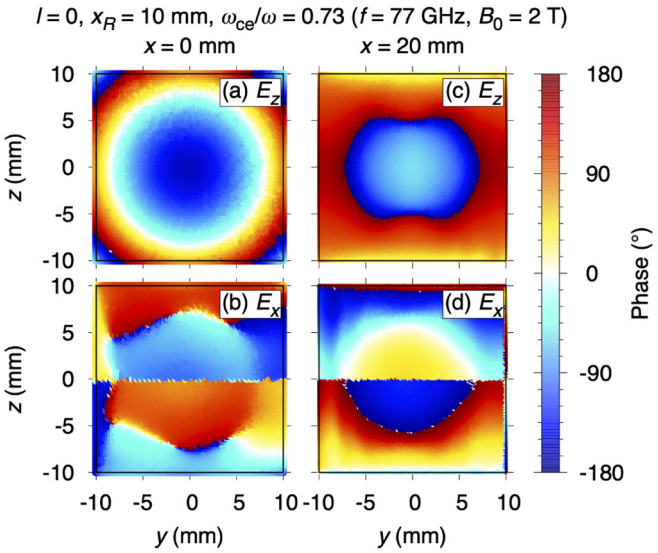

FIG. 33. Phase distributions of (a) and (c) E_z and (b) and (d) E_x on the y-z planes at (a) and (b) $x = 0$ mm and (c) and (d) $x = 20$ mm in the case of $l = 0$. Note that the phase distribution of E_z at $x = 0$ follows the contours of the function $l\varphi$ mod 2π.

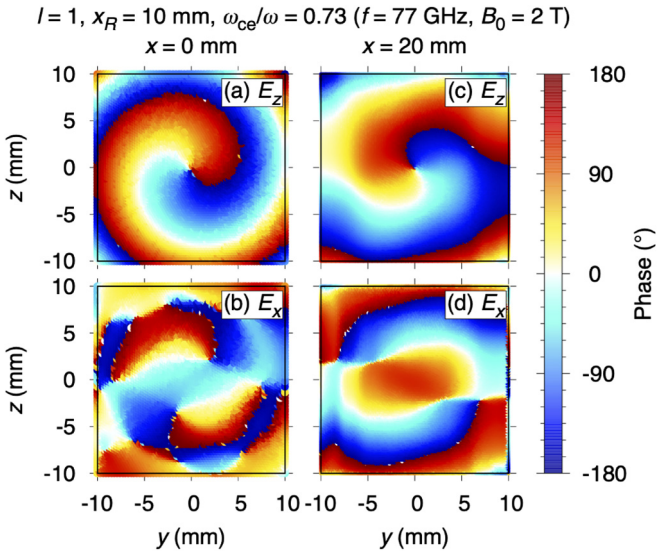

FIG. 35. Phase distributions of (a) and (c) E_z and (b) and (d) E_x on the y-z planes at (a) and (b) $x = 0$ mm and (c) and (d) $x = 20$ mm in the case of $l = 1$. Note that the phase distribution of E_z at $x = 0$ follows the contours of the function $l\varphi$ mod 2π.

at the R cutoff layer and cannot propagate through the evanescent region between the R cutoff layer and the UHR layer, so that the significant proportion of E_x shown in Fig. 34(b) is considered to be the X mode converted from the O mode. Figures 36 and 37 show the case of the LG beam excited with $l = 2$. In a manner similar to the case of $l = 1$, E_x with the high wavenumber is excited at the UHR layer. The topological charge of E_x is $l = 1$ around the propagation axis. Neither larger simulation boxes nor larger l can be processed at the moment due to limited computational resources.

IV. SUMMARY AND OUTLOOK

Propagation properties of EC waves with helical wavefronts are investigated theoretically in cold uniform magnetized plasma. The effects of the helical wavefront on the wave fields are described. These effects become significant as the topological charge of the vortex EC wave increases or the distance from the propagation axis becomes small. The different properties of propagation are also confirmed in COMSOL simulations with LG beams. It is found that a part of the O-mode LG beam with the topological charge l excited at the lower n_e region is converted into the high-wavenumber X-mode LG beam with l–1 at the UHR.

In order to demonstrate the new propagation properties of vortex EC waves in heating and current-drive experiments, an optical vortex with desired l must be generated in the millimeter-wave transmission system and launched into magnetic fusion plasma. A spiral-shaped mirror has been developed to generate an optical vortex with designed l in a frequency range of millimeter waves.[19] Thus, an optical vortex can be generated by installing the spiral-shaped mirror between a gyrotron and launching antenna mirrors in the existing transmission line. This enables verification of whether an optical vortex can be a tool to heat high-n_e plasma.

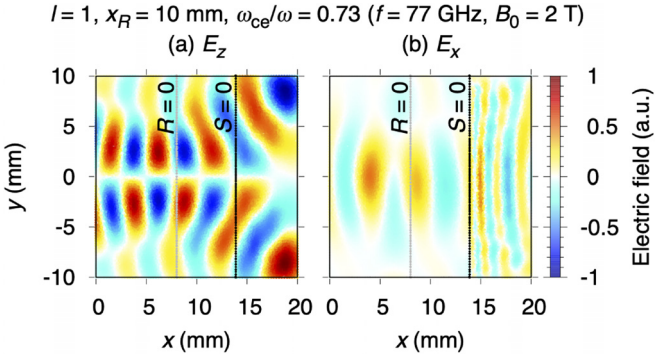

FIG. 34. Amplitude distributions of (a) E_z and (b) E_x on the x-y plane at $z = 0$ mm in the case of $l = 1$.

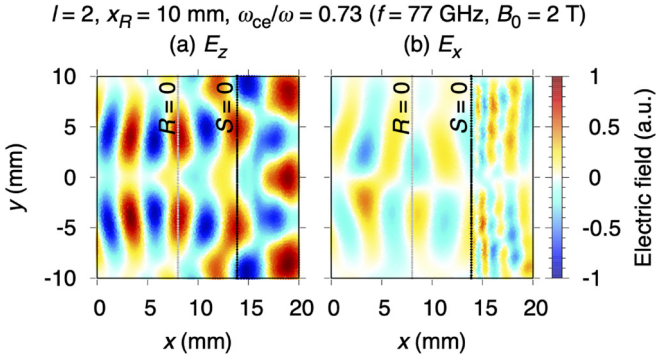

FIG. 36. Amplitude distributions of (a) E_z and (b) E_x on the x-y plane at $z = 0$ mm in the case of $l = 2$.

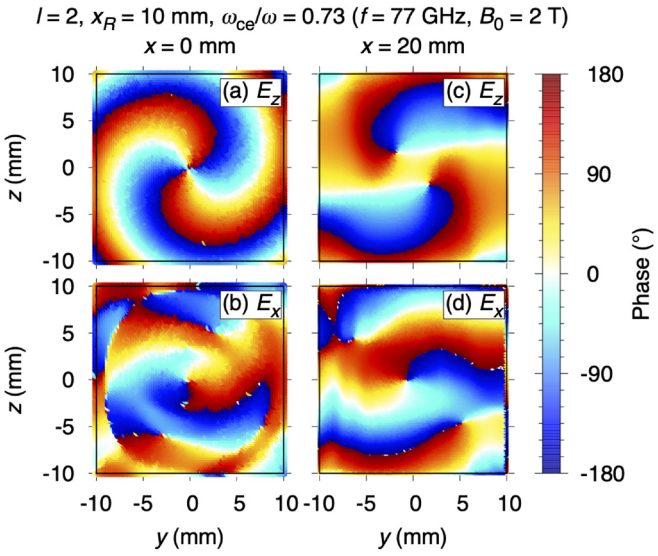

FIG. 37. Phase distributions of (a) and (c) E_z and (b) and (d) E_x on the y-z planes at (a) and (b) $x = 0$ mm and (c) and (d) $x = 20$ mm in the case of $l = 2$. Note that the phase distribution of E_z at $x = 0$ follows the contours of the function $l\varphi$ mod 2π.

ACKNOWLEDGMENTS

One of the authors, S.K., would like to thank Professor M. Katoh of Hiroshima University for continuous encouragement in investigating the propagation properties of the wave with OAM. We would like to thank anonymous referees for their careful reading of our manuscript and for their many insightful comments and suggestions. This work was supported by the NINS program for cross-disciplinary study (Grant Nos. 01311802 and 01311903), JSPS KAKENHI Grant No. JP19K14687, and NIFS Grant Nos. ULRR703 and ULRR036.

APPENDIX A: DIFFRACTION EFFECT IN EQ. (12)

In order to see the effect of diffraction, one can observe that, with $\boldsymbol{k}_R = \mathrm{Re}\boldsymbol{k}$ and $\boldsymbol{k}_I = \mathrm{Im}\boldsymbol{k}$, the components of $\boldsymbol{\Lambda}$ are

$$\Lambda_{mn}(\omega,\boldsymbol{k}) = \Lambda_{0,mn}(\omega,\boldsymbol{k}_R) - \frac{1}{2}(\boldsymbol{k}_I \otimes \boldsymbol{k}_I) : \frac{\partial^2 \Lambda_{0,mn}(\omega,\boldsymbol{k}_R)}{\partial \boldsymbol{k}_R \partial \boldsymbol{k}_R} + \mathrm{i}\boldsymbol{k}_I \cdot \frac{\partial \Lambda_{0,mn}(\omega,\boldsymbol{k}_R)}{\partial \boldsymbol{k}_R} + \mathrm{i}k_0^2 \varepsilon^a_{r,mn}, \tag{A1}$$

where

$$\boldsymbol{\Lambda}_0(\omega,\boldsymbol{k}_R) \equiv \boldsymbol{k}_R \otimes \boldsymbol{k}_R - (\boldsymbol{k}_R \cdot \boldsymbol{k}_R)\boldsymbol{I} + k_0^2 \boldsymbol{\varepsilon}_r^h$$

is the dispersion tensor including only real wave vector $\boldsymbol{k}_R$ and the Hermitian part $\boldsymbol{\varepsilon}_r^h$ of the dielectric tensor. Here, the symbol : in Eq. (A1) denotes the double dot product for two dyadics. Since $\boldsymbol{\Lambda}_0$ and its derivatives are Hermitian tensors, two anti-Hermitian contributions are identified. One is due to $\boldsymbol{k}_I$ and has to do with the amplitude factor $r^{|l|}$. The other one is the standard anti-Hermitian part of $\boldsymbol{\varepsilon}_r$, which accounts for dissipation, and is neglected in cold plasma away from EC resonances in the present analysis. The imaginary part $\boldsymbol{k}_I$ contributes to the Hermitian part as well. Such contributions are known in complex eikonal theory to deform the dispersion manifold in order to account for diffraction of the inhomogeneous wave. The present analysis is only limited under the ordering assumptions, where the effect of diffraction for long distance propagation is out of scope in z beyond $z \sim L$.

APPENDIX B: POYNTING VECTOR AND ENERGY CONSERVATION

From the wave electric field in Eq. (3), one finds

$$\nabla \times \boldsymbol{E} = \frac{1}{2}\left\{(\mathrm{i}\boldsymbol{k} \times \tilde{\boldsymbol{E}} + \nabla \times \tilde{\boldsymbol{E}})s + \mathrm{c.c.}\right\},$$

where $\boldsymbol{k} = -\mathrm{i}(|l|/r)\nabla r + l\nabla\varphi + k_z \nabla z$ and $s = \alpha r^{|l|}\exp[\mathrm{i}(l\varphi + \psi - \omega t)]$. Faraday's law with $\omega \neq 0$ yields the magnetic field amplitude

$$\tilde{\boldsymbol{B}} = \omega^{-1}(\boldsymbol{k} \times \tilde{\boldsymbol{E}} - \mathrm{i}\nabla \times \tilde{\boldsymbol{E}}).$$

The average in time over a wave period of $\boldsymbol{E} \times \boldsymbol{B}$ is

$$\begin{aligned}\overline{\boldsymbol{E} \times \boldsymbol{B}} &= \frac{1}{4}\left(\tilde{\boldsymbol{E}} \times \tilde{\boldsymbol{B}}^* + \tilde{\boldsymbol{E}}^* \times \tilde{\boldsymbol{B}}\right)|\alpha|^2 r^{2|l|}\mathrm{e}^{-2\mathrm{Im}\psi} \\ &\approx \frac{1}{4\omega}\left\{\tilde{\boldsymbol{E}} \times (\boldsymbol{k} \times \tilde{\boldsymbol{E}}^*) + \tilde{\boldsymbol{E}}^* \times (\boldsymbol{k} \times \tilde{\boldsymbol{E}}^*)\right\}|\alpha|^2 r^{2|l|}\mathrm{e}^{-2\mathrm{Im}\psi} \\ &\approx \frac{1}{4\omega}\left\{|\tilde{\boldsymbol{E}}|^2(\boldsymbol{k} + \boldsymbol{k}^*) - (\tilde{\boldsymbol{E}}^* \cdot \boldsymbol{k})\tilde{\boldsymbol{E}} - (\tilde{\boldsymbol{E}} \cdot \boldsymbol{k}^*)\tilde{\boldsymbol{E}}^*\right\} \\ &\quad \times |\alpha|^2 r^{2|l|}\mathrm{e}^{-2\mathrm{Im}\psi},\end{aligned}$$

where $\nabla \times \tilde{\boldsymbol{E}}$ has been neglected in the expression for the magnetic field amplitude. Then, in SI units,

$$\begin{aligned}\boldsymbol{S} &= \frac{1}{\mu_0}\overline{\boldsymbol{E} \times \boldsymbol{B}} \\ &\approx \frac{1}{4c\mu_0}\left\{|\tilde{\boldsymbol{E}}|^2(\boldsymbol{n} + \boldsymbol{n}^*) - (\tilde{\boldsymbol{E}}^* \cdot \boldsymbol{n})\tilde{\boldsymbol{E}} - (\tilde{\boldsymbol{E}} \cdot \boldsymbol{n}^*)\tilde{\boldsymbol{E}}^*\right\} \\ &\quad \times |\alpha|^2 r^{2|l|}\mathrm{e}^{-2\mathrm{Im}\psi},\end{aligned}$$

where $\boldsymbol{n} = c\boldsymbol{k}/\omega$.

Energy conservation follows by computing directly the divergence of this Poynting vector. Upon neglecting derivatives of $\boldsymbol{k}$ as well as those of $\tilde{\boldsymbol{E}}$ under the ordering assumptions, one computes

$$\begin{aligned}\nabla \cdot \boldsymbol{S} &\approx \frac{|\alpha|^2}{4\mu_0\omega}\nabla(r^{2|l|}\mathrm{e}^{-2\mathrm{Im}\psi}) \\ &\quad \times \left\{2|\tilde{\boldsymbol{E}}|^2\boldsymbol{k}_R - (\tilde{\boldsymbol{E}}^* \cdot \boldsymbol{k})\tilde{\boldsymbol{E}} - (\tilde{\boldsymbol{E}} \cdot \boldsymbol{k}^*)\tilde{\boldsymbol{E}}^*\right\} \\ &\approx -\frac{|\alpha|^2}{2\mu_0\omega}\boldsymbol{k}_I \cdot \left\{2|\tilde{\boldsymbol{E}}|^2\boldsymbol{k}_R - (\tilde{\boldsymbol{E}}^* \cdot \boldsymbol{k})\tilde{\boldsymbol{E}} - (\tilde{\boldsymbol{E}} \cdot \boldsymbol{k}^*)\tilde{\boldsymbol{E}}^*\right\} \\ &\quad \times r^{2|l|}\mathrm{e}^{-2\mathrm{Im}\psi},\end{aligned}$$

where the following identity is used:

$$\begin{aligned}\nabla(r^{2|l|}\mathrm{e}^{-2\mathrm{Im}\psi}) &= 2\left\{\frac{|l|}{r}\nabla r - \mathrm{Im}(k_z \nabla z)\right\}r^{2|l|}\mathrm{e}^{-2\mathrm{Im}\psi} \\ &= -2\boldsymbol{k}_I r^{2|l|}\mathrm{e}^{-2\mathrm{Im}\psi}.\end{aligned}$$

One can also observe that

$$\boldsymbol{k}_I \cdot \left\{(\tilde{\boldsymbol{E}}^* \cdot \boldsymbol{k})\tilde{\boldsymbol{E}} + (\tilde{\boldsymbol{E}} \cdot \boldsymbol{k}^*)\tilde{\boldsymbol{E}}^*\right\} = \tilde{\boldsymbol{E}}^* \cdot (\boldsymbol{k}_I \otimes \boldsymbol{k}_R + \boldsymbol{k}_R \otimes \boldsymbol{k}_I) \cdot \tilde{\boldsymbol{E}}$$

along with the identity

$$\boldsymbol{k}_I \cdot \frac{\partial \boldsymbol{\Lambda}_0(\omega, \boldsymbol{k}_R)}{\partial \boldsymbol{k}_R} = \boldsymbol{k}_I \otimes \boldsymbol{k}_R + \boldsymbol{k}_R \otimes \boldsymbol{k}_I - 2(\boldsymbol{k}_I \cdot \boldsymbol{k}_R)\boldsymbol{I}.$$

With some abuse of notation, on the left-hand side and in the following similar expressions the dot-product denotes contraction of the $\boldsymbol{k}$ indices, that is

$$\left\{\boldsymbol{k}_I \cdot \frac{\partial \boldsymbol{\Lambda}_0(\omega, \boldsymbol{k}_R)}{\partial \boldsymbol{k}_R}\right\}_{mn} = \boldsymbol{k}_I \cdot \frac{\partial \Lambda_{0,mn}(\omega, \boldsymbol{k}_R)}{\partial \boldsymbol{k}_R}.$$

The combination of the foregoing identities gives

$$\nabla \cdot \boldsymbol{S} \approx \frac{|\alpha|^2 r^{2|l|} \mathrm{e}^{-2\mathrm{Im}\psi}}{2\mu_0 \omega} \tilde{\boldsymbol{E}}^* \cdot \left\{\boldsymbol{k}_I \cdot \frac{\partial \boldsymbol{\Lambda}_0(\omega, \boldsymbol{k}_R)}{\partial \boldsymbol{k}_R}\right\} \cdot \tilde{\boldsymbol{E}}.$$

In general, the right-hand side is neither zero nor related to the dissipation of the wave. However, if it is assumed that $\boldsymbol{k}$ and $\tilde{\boldsymbol{E}}$ are chosen so that $\boldsymbol{\Lambda}(\omega, \boldsymbol{k}) \cdot \tilde{\boldsymbol{E}} = \boldsymbol{0}$ is satisfied. Then, multiplication on the left by $\tilde{\boldsymbol{E}}^*$ and the identity in Eq. (A1) give

$$\begin{aligned}\tilde{\boldsymbol{E}}^* \cdot \boldsymbol{\Lambda}(\omega, \boldsymbol{k}) \cdot \tilde{\boldsymbol{E}} = \tilde{\boldsymbol{E}}^* \cdot \boldsymbol{\Lambda}_0(\omega, \boldsymbol{k}_R) \cdot \tilde{\boldsymbol{E}} - \tilde{\boldsymbol{E}}^* \\ \cdot \left\{\frac{1}{2}(\boldsymbol{k}_I \otimes \boldsymbol{k}_I) : \frac{\partial^2 \boldsymbol{\Lambda}_0(\omega, \boldsymbol{k}_R)}{\partial \boldsymbol{k}_R \partial \boldsymbol{k}_R}\right\} \cdot \tilde{\boldsymbol{E}} \\ + \mathrm{i}\tilde{\boldsymbol{E}}^* \cdot \left\{\boldsymbol{k}_I \cdot \frac{\partial \boldsymbol{\Lambda}_0(\omega, \boldsymbol{k}_R)}{\partial \boldsymbol{k}_R}\right\} \cdot \tilde{\boldsymbol{E}} + \mathrm{i}k_0^2 \tilde{\boldsymbol{E}}^* \cdot \boldsymbol{\varepsilon}_r^a \cdot \tilde{\boldsymbol{E}} \\ = 0.\end{aligned}$$

The real and imaginary parts of this expression can be separated. The imaginary part, in particular, gives

$$\tilde{\boldsymbol{E}}^* \cdot \left\{\boldsymbol{k}_I \cdot \frac{\partial \boldsymbol{\Lambda}_0(\omega, \boldsymbol{k}_R)}{\partial \boldsymbol{k}_R}\right\} \cdot \tilde{\boldsymbol{E}} + k_0^2 \tilde{\boldsymbol{E}}^* \cdot \boldsymbol{\varepsilon}_r^a \cdot \tilde{\boldsymbol{E}} = 0.$$

Therefore, for solutions of Eq. (3), the energy balance becomes

$$\nabla \cdot \boldsymbol{S} \approx -k_0^2 \frac{|\alpha|^2 r^{2|l|} \mathrm{e}^{-2\mathrm{Im}\psi}}{2\mu_0 \omega} \tilde{\boldsymbol{E}}^* \cdot \boldsymbol{\varepsilon}_r^a \cdot \tilde{\boldsymbol{E}}.$$

DATA AVAILABILITY

The data that support the findings of this study are available within the article.

REFERENCES

[1] D. G. Swanson, *Plasma Waves*, 2nd ed. (Institute of Physics Publishing, Bristol and Philadelphia, 2003).
[2] I. Y. Dodin, D. E. Ruiz, K. Yanagihara, Y. Zhou, and S. Kubo, Phys. Plasmas **26**, 072110 (2019).
[3] M. Katoh, M. Fujimoto, H. Kawaguchi, K. Tsuchiya, K. Ohmi, T. Kaneyasu, Y. Taira, M. Hosaka, A. Mochihashi, and Y. Takashima, Phys. Rev. Lett. **118**, 094801 (2017).
[4] L. Allen, M. W. Beijersbergen, R. J. C. Spreeuw, and J. P. Woerdman, Phys. Rev. A **45**, 8185 (1992).
[5] M. Padgett, J. Courtial, and L. Allen, Phys. Today **57**(5), 35 (2004).
[6] M. Katoh, M. Fujimoto, N. S. Mirian, T. Konomi, Y. Taira, T. Kaneyasu, M. Hosaka, N. Yamamoto, A. Mochihashi, Y. Takashima, K. Kuroda, A. Miyamoto, K. Miyamoto, and S. Sasaki, Sci. Rep. **7**, 6130 (2017).
[7] S. Matsuba, K. Kawase, A. Miyamoto, S. Sasaki, M. Fujimoto, T. Konomi, N. Yamamoto, M. Hosaka, and M. Katoh, Appl. Phys. Lett. **113**, 021106 (2018).
[8] T. Kaneyasu, Y. Hikosaka, M. Fujimoto, H. Iwayama, M. Hosaka, E. Shigemasa, and M. Katoh, J. Synchrotron Radiat. **24**, 934 (2017).
[9] T. Ii Tsujimura, S. Kubo, H. Takahashi, R. Makino, R. Seki, Y. Yoshimura, H. Igami, T. Shimozuma, K. Ida, C. Suzuki, M. Emoto, M. Yokoyama, T. Kobayashi, C. Moon, K. Nagaoka, M. Osakabe, S. Kobayashi, S. Ito, Y. Mizuno, K. Okada, A. Ejiri, T. Mutoh, and LHD Experiment Group, Nucl. Fusion **55**, 123019 (2015).
[10] N. B. Marushchenko, Y. Turkin, and H. Maassberg, Comput. Phys. Commun. **185**, 165 (2014).
[11] Y. Goto, S. Kubo, and T. I. Tsujimura, J. Adv. Simul. Sci. Eng. **7**, 34 (2020).
[12] T. Takahashi, Kogaku (Jpn. J. Opt.) **47**, 30 (2018) (in Japanese), http://myosj.or.jp/wp-content/themes/osj/download/kogaku/47-1/07.pdf.
[13] T. H. Stix, *Waves in Plasmas* (American Institute of Physics, New York, 1992).
[14] H. Takahashi, T. Shimozuma, S. Kubo, Y. Yoshimura, H. Igami, S. Ito, S. Kobayashi, Y. Mizuno, K. Okada, T. Mutoh, K. Nagaoka, S. Murakami, M. Osakabe, I. Yamada, H. Nakano, M. Yokoyama, T. Ido, A. Shimizu, R. Seki, K. Ida, M. Yoshinuma, T. Kariya, R. Minami, T. Imai, N. B. Marushchenko, Y. Turkin, and LHD Experiment Group, Phys. Plasmas **21**, 061506 (2014).
[15] See https://www.comsol.com for Simulate real-world designs, devices, and processes with multiphysics software from COMSOL.
[16] T. Mori, M. Nishiura, Z. Yoshida, N. Kenmochi, S. Katsura, K. Nakamura, Y. Yokota, T. I. Tsujimura, and S. Kubo, Plasma Fusion Res. **14**, 3401134 (2019).
[17] S. Shiraiwa, O. Meneghini, R. Parker, P. Bonoli, M. Garrett, M. C. Kaufman, J. C. Wright, and S. Wukitch, Phys. Plasmas **17**, 056119 (2010).
[18] C. Lau, L. A. Berry, E. F. Jaeger, and N. Bertelli, Plasma Phys. Controlled Fusion **61**, 045008 (2019).
[19] Y. Goto, T. I. Tsujimura, and S. Kubo, J. Infrared Millimeter Terahertz Waves **40**, 943 (2019).